

University of Southern Queensland
Faculty of Health, Engineering & Sciences

**Drag reduction and wake mitigation in wind turbines using
riblet microstructures**

A dissertation submitted by

Daniel J. McEvoy

in fulfilment of the requirements of

ENG4112 Research Project

towards the degree of

Bachelor of Mechanical Engineering (Hons)

Submitted: Oct, 2020

Abstract

Wind turbines suffer many inefficiencies under immensely dynamic conditions. Turbulence, whether systemic or deliberately induced, generates far wake fields that deplete kinetic energy for downstream installations. This study will examine the use of a geometrical feature known as ‘riblets’, applied to the surface of turbine blades to reduce drag and mitigate wake effects.

Riblets were inspired by dermal denticles in shark skin, capable of reducing shear forces in the boundary layer. Previous studies into the use of man-made riblets focused on uniform designs across the aerofoil without giving consideration to bespoke designs that would address the complex varying shear forces and turbulent kinetic energy regions of the boundary layer. Computational fluid dynamic software was used to validate a known NACA 0012 aerofoil against experimental and simulated values from the National Aeronautics and Space Administration (NASA). Variations were then made to both uniform and non-uniform riblet configurations ranging in size from 50 to 125 micrometers along the chord length of an NACA 0012 standard symmetrical aerofoil. These included uniform and non-uniform riblet designs from fore to aft chordwise.

3D simulations were completed using SOLIDWORKS Flow Simulation to measure free stream velocity and static/dynamic pressures across eight (8) aerofoils at wind speeds ranging from 5-90 m/s. A further four (4) S-802 wind turbine blade aerofoils were modelled and the methodology repeated. Comparing drag coefficients resulted in an overall decrease in performance of the riblet aerofoils, contrary to previous experimental studies. Drag was greater by up to 20% at lower velocities with the detriment decreasing as wind velocity increased.

It is likely that computational fluid dynamic software is unable to account for the complex nature of vortex control in the boundary layer. Whilst it may be able to resolve the

generation and estimate the effects, when considering that the underlying mechanism for raising, pinning and separating vortices is not completely understood in experimentation, it would follow that software packages are yet to incorporate what is still a somewhat unknown phenomenon and it is likely cost prohibitive to develop.

This document describes the development of the project from original idea initiation to a fully scoped research project and resultant findings. This proposal includes a comprehensive literature review, proposed methodology of research, project scheduling, costs, risk assessment, risk mitigation and quality control planning. This research reaffirms the lack of precise understanding as to exactly why experimental riblet designs are able to yield drag reductions. Despite there being very reasonable assumptions it is likely still beyond even very complex CFD software algorithms. The research therefore indicates that in order to apply knowledge to wind turbine blade design, experimental data is not expected to corroborate simulations and practical application for research should be the starting point for drag reduction and the control of turbulent vortex generation in the field of fluid mechanics until greater practical understanding is achieved.

University of Southern Queensland
Faculty of Health, Engineering & Sciences

ENG4111/2 *Research Project*

Limitations of Use

The Council of the University of Southern Queensland, its Faculty of Health, Engineering & Sciences, and the staff of the University of Southern Queensland, do not accept any responsibility for the truth, accuracy or completeness of material contained within or associated with this dissertation.

Persons using all or any part of this material do so at their own risk, and not at the risk of the Council of the University of Southern Queensland, its Faculty of Health, Engineering & Sciences or the staff of the University of Southern Queensland.

This dissertation reports an educational exercise and has no purpose or validity beyond this exercise. The sole purpose of the course pair entitled “Research Project” is to contribute to the overall education within the student’s chosen degree program. This document, the associated hardware, software, drawings, and other material set out in the associated appendices should not be used for any other purpose: if they are so used, it is entirely at the risk of the user.

Dean

Faculty of Health, Engineering & Sciences

Certification of Dissertation

I certify that the ideas, designs and experimental work, results, analyses and conclusions set out in this dissertation are entirely my own effort, except where otherwise indicated and acknowledged.

I further certify that the work is original and has not been previously submitted for assessment in any other course or institution, except where specifically stated.

DANIEL J. MCEVOY



Acknowledgments

I wish to acknowledge the ever evolving character within myself over the past 8 years of this transformative process, for no others have provided such support or undying commitment to the progression of this educational milestone. It would be remiss not to thank the person I was each previous year, whose differing mindset, abilities, finances, relationships, country of living and career changes had this common goal and alone persevered until the end.

I also wish to thank the ongoing guidance and wisdom and the positive encouragement provided by my supervisor Dr. Khalid Saleh of the University of Southern Queensland. Without his help I may not have persevered through the challenging barriers both on technical and personal levels over the past year.

DANIEL J. MCEVOY

Contents

Abstract	i
Acknowledgments	v
List of Figures	xi
List of Tables	xiv
Abbreviations and Acronyms	xv
Chapter 1 Introduction	1
1.1 Aims, objectives and scope	2
1.2 Overview of the Dissertation	3
Chapter 2 Literature Review	4
2.1 Wind turbine blade design	4
2.1.1 Wind Energy Equation	4
2.1.2 Betz Limit	5
2.1.3 Tangential Speed and Increased Complexity of a Rotating aerofoil	6

2.1.4	Power Coefficient	6
2.2	Aerofoil turbulence and wake effects	7
2.2.1	Near Wake Region	8
2.2.2	Far Wake Region	8
2.2.3	Offshore Installations	9
2.3	Riblet design and aerofoil selection	9
2.3.1	Nature's Answer - Shark Skin Dermal Denticles	10
2.3.2	Proposed Reasoning for Phenomenon	10
2.3.3	Synthetic Riblet Geometries	12
2.4	NACA 0012 Aerofoil selection	12
2.5	Research need and justification	13
2.5.1	Experiments Using Uniform Riblets	13
2.5.2	Proposed Non-uniform Riblet Designs	14
2.5.3	Shear Stress and Kinetic Energy Distribution Along an Aerofoil	14
2.5.4	Environmental and social impact	16
2.6	Literature Review for Further Research	17
2.6.1	3D Prototype Printing	17
2.6.2	Wind Tunnel Considerations	18
Chapter 3 Research Methodology		22
3.1	Project Development	22
3.1.1	Procedure for Modelling and Simulations	22

3.1.2	Limitations	24
3.1.3	Expected outcomes and benefits	25
3.2	Project Planning	26
3.2.1	Resource Requirements	26
3.2.2	Project Schedule	27
3.2.3	Risk Assessment	27
3.2.4	Quality Assurance Plan	27
Chapter 4 Numerical Analysis		33
4.1	Governing Equations	33
4.2	SOLIDWORKS Equations	35
4.2.1	Thin-Boundary-Layer approach	40
4.2.2	Thick-Boundary-Layer approach	40
4.3	Input Parameters for Validation (NASA)	41
4.4	Mesh Refinement Process	41
4.4.1	Initial Mesh	42
4.4.2	Domain Refinement	43
4.4.3	Global Mesh Refinement	45
4.4.4	Advanced Mesh Refinement	46
4.4.5	Final Mesh Model Selection	49
4.5	Proposed Research Model	51

Chapter 5 Results and Discussion	56
5.1 NACA 0012 Model	57
5.2 S-802 Wind Turbine Blade Model	58
5.3 Discussion	59
Chapter 6 Conclusions and Further Work	60
6.1 Conclusions	60
6.2 Further Work	61
References	62
Appendix A Project Specification	68
Appendix B Raw Data Sets	70
B.1 Domain Mesh Optimisation	71
B.2 Advanced Mesh Criterion Optimisation Data	72
B.3 Final Mesh Model Refinements	74
B.4 NACA 0012 Riblet Performance	75
B.5 S-802 Riblet Performance	76

List of Figures

1.1	Historical development of primary energy supply from renewable energy	2
2.1	Circular tube of air flowing through ideal wind turbine	5
2.2	Definition of pitch angle β and angle of attack γ	6
2.3	Relationships of $C_{p,max}$ with ϵ for the optimal design	7
2.4	Flow visualization with smoke	8
2.5	Two NREL 5-MW turbines subjected to NL atmospheric conditions	9
2.6	Scale patterns of fast sharks showing riblet formations	10
2.7	Turbulent vortices interaction with riblets (flow into page, to relative scale)	11
2.8	Common riblet geometries (cross sectional views)	12
2.9	Wind tunnel airflow and angle of attack	14
2.10	Variation of Reynolds shear stress distribution (RE=1.54x10 ⁴)	15
2.11	Variation of turbulent kinetic energy distribution (RE=1.54x10 ⁴)	15
2.12	Distribution of Reynolds numbers with length of blade for 6 common wind turbines	19
3.1	Proposed riblet geometry overview	23

3.2	Riblet spacing to maintain height to spacing ratio	24
4.1	Averaged turbulence velocity profile	33
4.2	Normal and shear stresses on fluid particle	35
4.3	Common types of mesh construction	36
4.4	SOLIDWORKS Mach Number flow field	39
4.5	3D plot of NACA0012 aerofoil	42
4.6	Basic, non-uniform global mesh (sectional plane x-x)	43
4.7	Domain refinement by boundary	44
4.8	Global mesh - software auto-refinement level 6	45
4.9	Increasing accuracy with successive global mesh refinements	46
4.10	Refining specific advanced mesh criteria and the effect on the coefficient of drag	48
4.11	Increasing computing cost with diminishing returns	48
4.12	Evaluation of final mesh models with consideration to computational time	50
4.13	Figure 4.12 extended to show FMM1 further refinement	50
4.14	Pressure variation along chord length	53
4.15	Turbulent kinetic energy along chord length	53
4.16	Example of non-uniform riblet design travelling chordwise along an aerofoil surface	54
4.17	Aerofoil section with longitudinal riblets	54
4.18	S-802 aerofoil section with 50 μ m-125 μ m riblets	55

5.1 NACA 0012 Riblet performance under varying wind speeds 57

5.2 S-802 Riblet performance under varying wind speeds 58

List of Tables

3.1	Resource requirements	26
3.2	Project Task Descriptions	28
3.3	Project Schedule	29
3.4	Risk Assessment Matrix	30
3.5	Risk Assessment	31
3.6	Risk Assessment (continued)	32
4.1	Scenarios for comparison in selecting optimised mesh	49
4.2	Sawtooth riblet airfoil experimentation	52
B.1	Domain Mesh Optimisation Data	71
B.2	Advanced Mesh Criterion Optimisation Data	72
B.2	Advanced Mesh Criterion Optimisation Data (continued)	73
B.3	Final Mesh Model Optimisation Data	74
B.4	NACA 0012 Riblet Performance Data	75
B.5	S-802 Riblet Performance Data	76

Abbreviations and Acronyms

ABS	Acrylonitrile Butadiene Styrene
BEM	Blade Element/Momentum theory
CFD	Computational Fluid Dynamics
FDM	Fused Deposition Modelling
HAWT	Horizontal Axis Wind Turbine
MIT	Massachusetts Institute of Technology
MJM	Multi-Jet Modelling
NACA	National Advisory Committee for Aeronautics
PLA	Polylactic Acid
RANS	Reynolds-averaged Navier-Stokes equations
RSPB	The Royal Society for the Protection of Bird
SLA	Stereolithography apparatus
SLS	Selective Laser Sintering
TUSQ/USQ	The University of Southern Queensland

Chapter 1

Introduction

This research seeks to improve the design of wind turbine blades and further advance renewable energy technology. The Intergovernmental Panel on Climate Change (IPCC 2012, 33) reports that ‘most of the observed increase in global average temperature since the mid-20th century is very likely due to the observed increase in anthropogenic greenhouse gas concentrations’ but that it ‘may also contribute to social and economic development, energy access, a secure energy supply, and reducing negative impacts on the environment and health’ (IPCC 2012, 7). Renewable energy technology is well-known to reduce greenhouse gas concentrations.

Twidell & Weir (2015) explain that renewable energy was once seen only as an appropriate and intermediate technology but with the rise of coupling technologies such as composite materials, computer-aided design and smart technology, commercial-scale applications are not only common but incorporated into major utility divisions. Renewable energy examples include biofuels, solar, geothermal and wind energy. In Figure 1 below, we see the rapid growth in wind energy. Wind energy is growing faster than most alternatives and is the focus for this project.

A literature review into wind turbine technology explores many concepts including optimum rotor blade design, geographical locality, terrain placement, hub height and material selection. Significant energy capture inefficiencies occur through turbulence created by Horizontal Axis Wind Turbines (HAWTs) aft of the rotor diameter. A potential gap was identified relating to the design of ‘riblets’ as a means of improving laminar flow and reducing shear stresses in the boundary layer airflow.

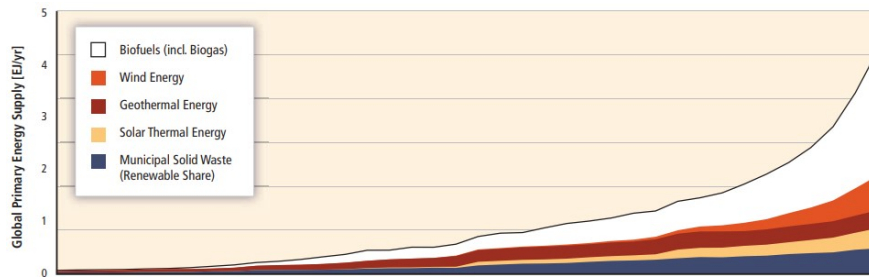


Figure 1.1: Historical development of primary energy supply from renewable energy from 1971 to 2008. (IPCC 2012, 11).

A typical NACA 0012 symmetrical aerofoil will be modelled using Autodesk Inventor CAD software and analysed using SOLIDWORKS Flow Simulation. Several design variations of riblets will be applied to the model and the analysis repeated. Findings will be interpreted and successful designs applied to a standard S-802 wind turbine blade and further analysis conducted.

This project focuses on fluid mechanics relating to Horizontal Axis Wind Turbines (HAWTS) and is relevant to many industries including aviation, hydroelectrical and medical.

1.1 Aims, objectives and scope

The aim of this project is to analyse the performance of several variations in riblet design along the chord length of a standard aerofoil. The project will help to validate the hypothesis that a non-uniform riblet geometry will perform better than a uniform distribution in lowering drag. It also seeks to improve turbine startup and operation at lower wind speeds. In future studies this may benefit the wind energy sector of renewable technologies by improving wind turbine blade performance. The reduction of surface drag and improved lift characteristics means turbine farms will also perform better. Wind turbines capable of reaching maximum rotational velocity will still be regulated through induced stall conditions creating turbulence, but will do so at lower undisturbed wind speeds thereby reducing far field wake effects in wind farm clusters. This initial improvement therefore has a multiplying effect on energy output, applicable to both on and offshore installations. To ensure these aims are realized the following objectives are proposed for this project:

- To model and simulate an NACA 0012 aerofoil in CFD software as a base reference

of what could be expected from the ideal aerofoil without riblets

- To model and simulate at a minimum 4 NACA 0012 aerofoils – one smooth, one with previously studied $100\mu m$ uniform riblets and two additional aerofoils with differing riblet profile variations using CFD software
- To apply gained understandings to the creation of an S-802 wind turbine blade profile for simulation and analysis
- To analyse data and compare the outcomes against the original aims of this project
- To recognize required improvements to the study and suggest further research ideas,

The proposed scope of this study is limited to the NACA 0012 and S-802 aerofoils under tightly controlled conditions to minimize unknowns. Wind turbines exist in very complex fluid dynamic environments as highlighted in the literature review, however, the outcomes from this study may promulgate broader research scope if modelling or experimental data yields beneficial results. Applications are not limited to wind turbines but to all aspects of aviation both of rotary and fixed wing, and possibly marine environments where viscous fluid forces abide by similar principles. Alternatively, this project may provide valid reason to direct research effort and resources elsewhere.

1.2 Overview of the Dissertation

This dissertation is organized as follows:

Chapter 2 Literature Review

Chapter 3 Research Methodology

Chapter 4 Numerical Analysis

Chapter 5 Results and Discussion

Chapter 6 Conclusion and Further Work

Chapter 2

Literature Review

2.1 Wind turbine blade design

2.1.1 Wind Energy Equation

According to Schubel Schubel & Crossley (2012), classical approaches to wind turbine design relied on a drag factor (C_d). Designs such as cup anemometers worked by capturing wind forces on one face but reducing drag on the opposing face. Eventually the angular velocity reaches the wind velocity and the tip speed ratio cannot exceed 1. Rotor blades designed as aerofoils overcome this, but efficiency is limited. The maximum power attainable through wind kinetic energy given in Equation (2.1):

$$P_{max} = \frac{1}{2}\dot{m}V_o^2 = \frac{1}{2}\rho AV_o^3 \quad (2.1)$$

where \dot{m} is the mass flow rate, ρ is the density, A is the swept area and V is the air velocity.

Importantly the energy is the cube of the wind speed and far outweighs the linearly increasing density and area factors.

2.1.2 Betz Limit

As explained in Schubel Schubel & Crossley (2012), ‘100% extraction would require zero final velocity and zero flow which has led to the widely accepted principle that maximum wind turbine efficiency cannot exceed 59.3%’ and can be seen in Figure 1.2 below:

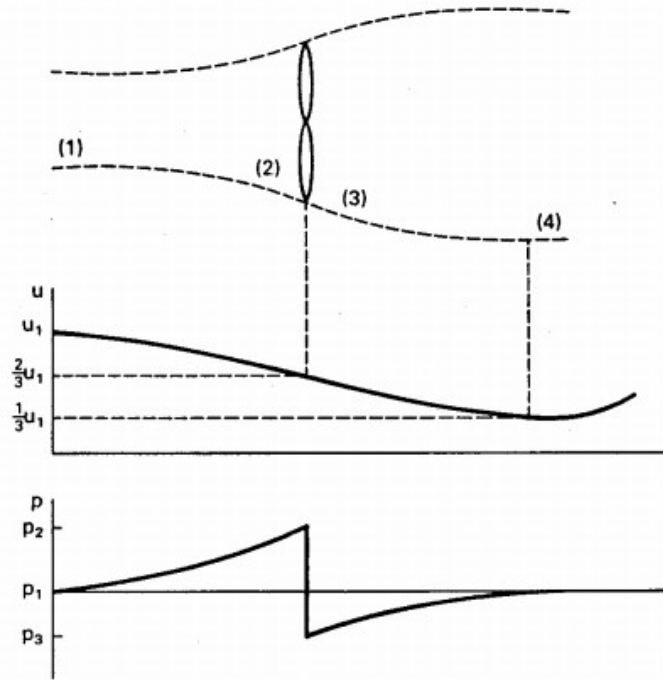


Figure 2.1: Circular tube of air flowing through ideal wind turbine. (Johnson 2006, 3).

As the wind approaches the turbine it is slowed by the blades and expands converting kinetic energy to potential energy to produce a pressure increase. Rearward, more kinetic energy is again converted to raise the pressure back to atmosphere (Johnson 2006, 3), represented by Equation (2.2):

$$P_{m,ideal} = \frac{1}{2}\rho\left[\frac{8}{9}\left(\frac{2}{3}A_2\right)u_1^3\right] = \frac{1}{2}\rho\left(\frac{16}{27}A_2u_1^3\right) \quad (2.2)$$

This is known as the Betz limit whereby the power coefficient $C_{p,max} = \frac{16}{27}$ i.e. 59.3%. According to Johnson Johnson (2006) this pressure difference across the turbine is very small, only 0.02 percent of the ambient pressure meaning small pressure changes have a substantial effect on turbine power outputs. This emphasizes the need to research methods of controlling the boundary layer.

2.1.3 Tangential Speed and Increased Complexity of a Rotating aerofoil

Next, it is important to recognize key differences between rotating wind turbine blades and standard aerofoils. An aircraft wing can be considered to undergo a steady flow of fluid across its aerofoil at varying angles of attack (α). However, as a wind turbine begins to rotate the approach vector of the wind shifts as a combination of the undisturbed incoming wind speed and the changing relative airflow. This is shown in figure 2.2:

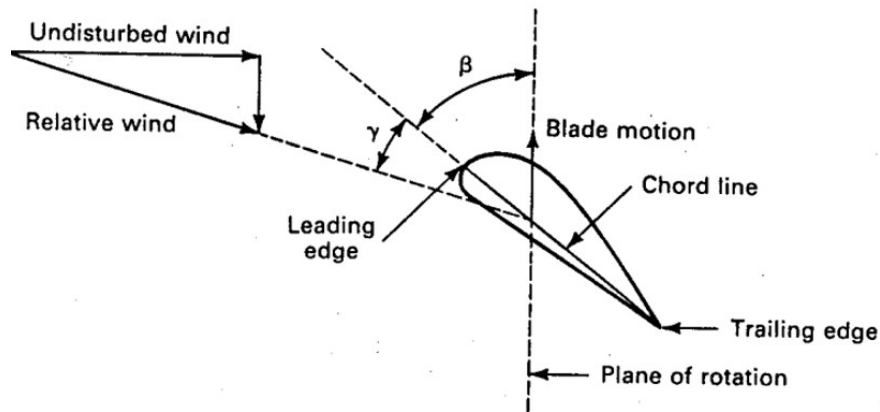


Figure 2.2: Definition of pitch angle β and angle of attack γ . (Johnson 2006, 6).

Factors affecting the performance are not constant and vary with wind speed, rotational speed, turbine blade parameters such as angle of attack and pitch angle. This means that varying values of C_p can be obtained at the same wind speed, necessitating a more convenient approach for developing a power curve. Experimentally, this value is defined as the tip-to-speed ratio:

$$\lambda = \frac{r_m \omega_m}{u} \quad (2.3)$$

where r_m is the maximum radius of the turbine, ω_m is the angular velocity of the turbine in rad/s and u is the undisturbed wind speed (Johnson 2006, 9).

2.1.4 Power Coefficient

Ge et al. (2016) showed that at a certain tip-to-speed ratio, the optimal power coefficient correlates only with the reciprocal of drag versus lift coefficients, $\epsilon(\frac{C_d}{C_l})$ as in Figure 2.3:

This can be fitted by a linear formula (2.4):

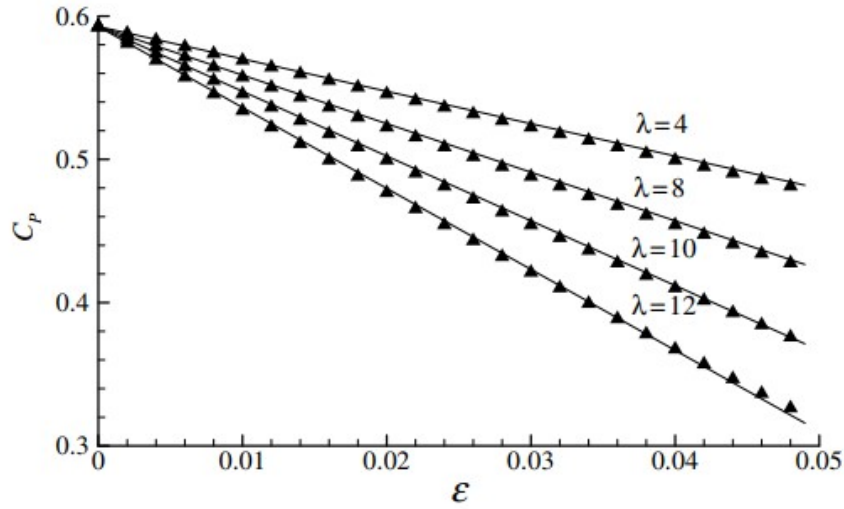


Figure 2.3: Relationships of $C_{p,max}$ with ϵ for the optimal design. (Ge et al. 2016, 6).

$$C_{p,max} = 0.593 - 0.565\lambda\epsilon \quad (2.4)$$

where the first term is the Betz limit, and the second term is the loss induced by drag. It shows that $C_{p,max}$ is reduced by drag approximately proportional to tip-speed ratio λ . Therefore, at a given tip speed ratio any additional drag reduction i.e. via riblets, will linearly increase power output.

2.2 Aerofoil turbulence and wake effects

The majority of aircraft aerofoils are designed predominantly for steady flow conditions outside the near-earth envelope, whereas wind turbines operate nearer to ground and endure characteristically unsteady conditions. This can generate large areas of wake. Wind turbine blades are also designed to harness stall conditions for velocity regulation adding further rearward turbulence. It is therefore worth investigating what effect riblets may have on wake intensity. According to Vermeer et al. (2003) the wake can be divided into two distinct regions, being the near and far wake regions.

2.2.1 Near Wake Region

The near wake exists just rear of the rotor by approximately one rotor diameter and becomes apparent due to the “number of blades, blade aerodynamics, including stalled flow, 3-D effects and tip vortices” (Vermeer et al. 2003, 469) and is depicted in Figure 2.4. Near wake computations are largely based on the blade element/momentum theory (BEM), relying on two-dimensional sectional aerofoil characteristics which have proven accurate for most common flow conditions, but are unable to account for complex stall conditions existing at high speed rotations where centrifugal forces and Coriolis pumping decreases boundary layer thickness.

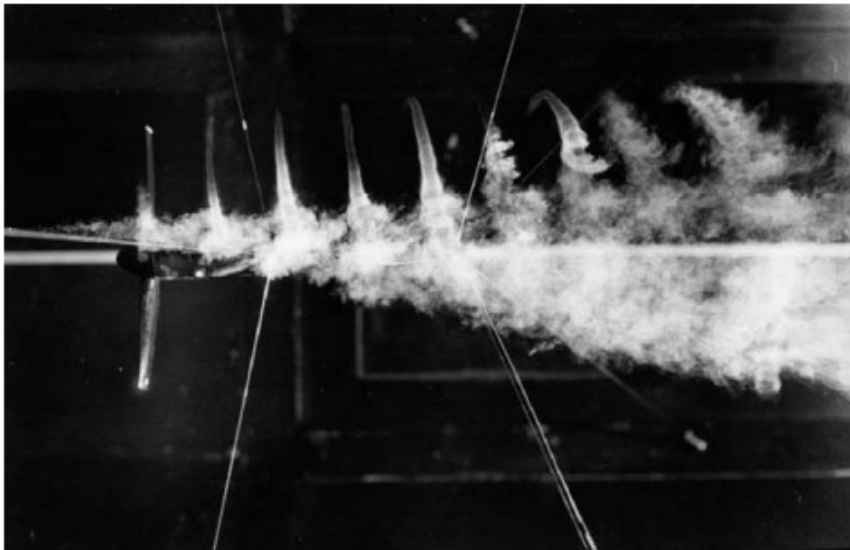


Figure 2.4: Flow visualization with smoke, revealing smoke trails being ‘sucked’ into vortex spirals. (Alfredsson & Dahlberg 1979).

2.2.2 Far Wake Region

The far wake occurs 2 to 5 diameters downstream as the shear layer reaches the wake axis (Vermeer et al. 2003, 489) and is detrimental in wind farm clusters where accumulating turbulence saps wind energy for the next turbine. Högström et al. (1988) measured a 2MW turbine to exhibit turbulence at 10.5 diameters on flat country in Sweden, this was emphasized in Højstrup (1999) reaching up to 14.5 diameters in smaller 300kW turbines in a Danish windfarm, thought due to aggregated wakes from many upstream turbines. The differences may be attributed to a number of factors such as location, singular turbine versus wind farm clusters, undisturbed wind speed at the operating locations, turbulence

intensity and many other factors but nonetheless supports the notion that far wake effects are pronounced in a variety of models. Figure 2.5 depicts a wake simulation from the National Renewable Energy Laboratory:

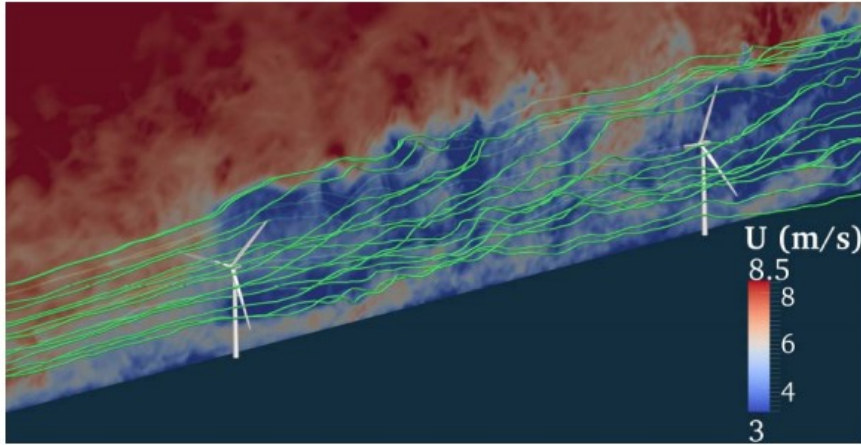


Figure 2.5: Two NREL 5-MW turbines subjected to NL atmospheric conditions showing the instantaneous streamwise velocity with streamlines (Lee et al. 2012, 6).

2.2.3 Offshore Installations

Chacón et al. (1996) identify amplified effects to offshore windfarms as wind travels from higher surface roughness land to much smaller ocean surface roughness, increasing wind velocity and turbulence intensities. This is supported again in Højstrup (1999) concluding that where ambient turbulence levels are lower, such as offshore, wakes could extend much farther downstream. By virtue of reducing drag effects, and by allowing turbines to reach operating conditions at lower wind velocities, this research into improving riblet designs may reduce wake effects. This is particularly beneficial to offshore applications.

2.3 Riblet design and aerofoil selection

In commercial transport applications, viscous or skin friction drag accounts for 40-50% of total drag under cruise conditions. Methods to overcome this generally involve delaying laminar-turbulent boundary layer transition or altering the turbulent structure of the turbulent boundary layer (Viswanath 2002, 572-3).

2.3.1 Nature's Answer - Shark Skin Dermal Denticles

Studies into why certain marine life such as whales accumulate barnacles whilst sharks do not, revealed dermal denticles in the direction of fluid flow of roughly $100\mu\text{m}$, shown in Figure 2.6.

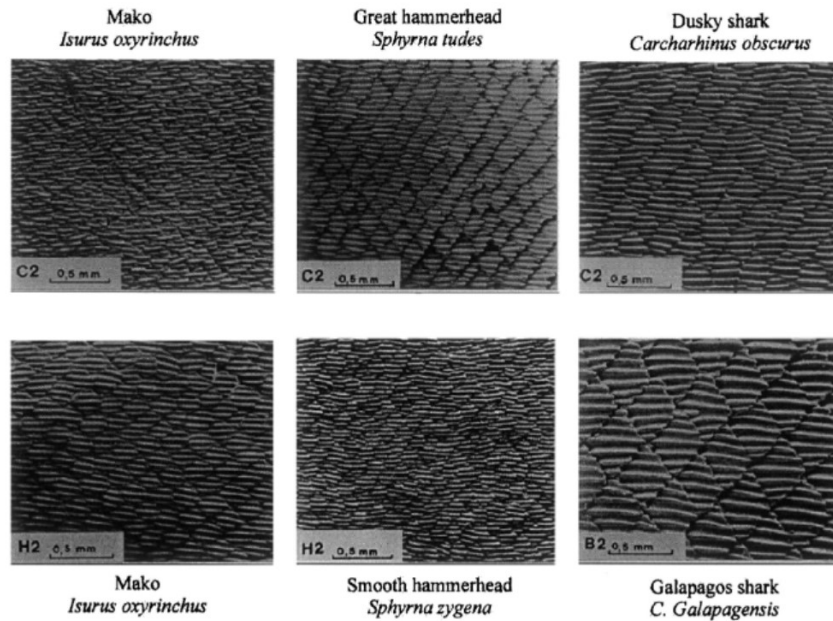


Figure 2.6: Scale patterns of fast sharks showing riblet formations (Fu et al. 2017, 18).

These microstructures control turbulent vortices at the solid liquid interface and reduce momentum transfer, shear stress and hence drag (Bixler & Bushan 2013, 4509).

2.3.2 Proposed Reasoning for Phenomenon

Sidhu et al. (2016) explain how these small riblets impede vortex cross-stream translation, decreasing the rate of vortex injection toward the outer region of the boundary layer. It is also well established that drag is related to total wetted surface area. Despite riblets increasing the surface area, the riblets pin the vortices to the riblet tips whilst maintaining low flow velocity in the valleys. This substantially reduces shear stress on the surface. This is visualised in Figure 2.7 below:

Turbulent vortices interaction with riblets
(flow into page, to relative scale)




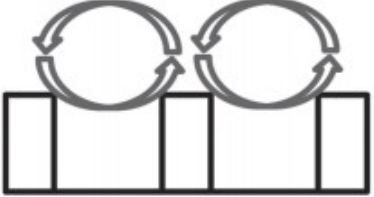
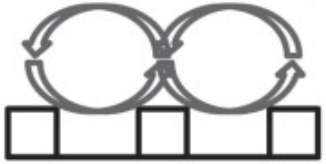
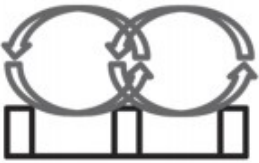
<p>Flat plate</p> 	<p>Vortices contact Surface area Entanglement Pinning Drag</p>
<p>Baseline (h, s, vw, t)</p> 	<p>Vortices contact ↓ Surface area ↑↑ Pinning ↑ Drag ↓</p>
<p>Shallow (½h, s, vw, t)</p> 	<p>Vortices contact ↓ Surface area ↑ Pinning ↑ Drag ↓↓</p>
<p>Deep (2h, s, vw, t)</p> 	<p>Vortices contact ↓ Surface area ↑↑↑ Pinning ↑ Drag ↑↑</p>
<p>Narrow (h, ⅔s, ¾vw, t)</p> 	<p>Vortices contact ↓ Surface area ↑↑ Entanglement ↑ Pinning ↓ Drag ↑</p>
<p>Thin (h, ¾s, vw, ½t)</p> 	<p>Vortices contact ↓ Surface area ↑↑ Entanglement ↑ Pinning ↓↓ Drag ↑</p>

Figure 2.7: Turbulent vortices interaction with riblets (flow into page, to relative scale) (Bixler & Bushan 2013, 4524).

2.3.3 Synthetic Riblet Geometries

Various riblet geometries have been experimented on including blade, sawtooth and scalloped many exhibiting around 8% maximum turbulent drag reduction (Bixler & Bushan 2013, 4512). Parameters include height (h), spacing (s), thickness (t) and valley width (vw) as in figure 2.8:

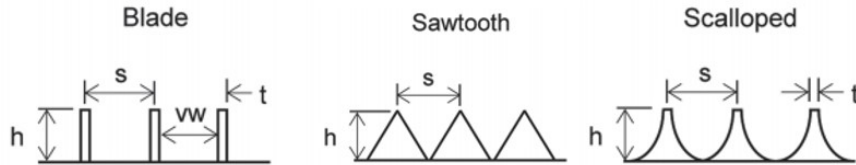


Figure 2.8: Common riblet geometries (cross sectional views) (Bixler & Bushan 2013, 18).

2.4 NACA 0012 Aerofoil selection

The aerofoil design proposed for this research is based of the National Advisory Committee for Aeronautics (NACA) which standardized the most successful parameters for aerofoils in the 1930's based off the shape of the slope of the aerofoil, the mean camber line and the thickness distribution above this line (Stanford University 2013). The 1st digit refers to maximum chamber to chord ratio, 2nd digit is the camber position in tenths of the chord and the 3rd & 4th digits are the maximum thickness to chord ratio in percent (Schubel & Crossley 2012, 3436).

According to Chamorro et al. (2013), despite the NACA 0012 not being used specifically in wind turbines, its performance is very well documented provides an excellent basis for comparative research into cases using riblets. As such it is commonly used in wind turbine blade optimization experiments as demonstrated by Rasal & Katwate (2017), Sidhu et al. (2016) and Chen, X. (2014), and is proposed for this research.

2.5 Research need and justification

2.5.1 Experiments Using Uniform Riblets

Experiments in drag reduction through riblet geometries were investigated by Chamorro et al. (2013). Experiments were performed on a full-scale 2.5MW wind turbine section by covering the surface partially or fully with riblets. Angles were tested between angles of attack (α)= 0° and 10° and $Re = 2.2 \times 10^6$. The drag was calculated by measuring the mean drag in the wake. In multiple cases the partial coverage was more efficient than the full coverage and in many cases the drag was reduced, however, in some they proved detrimental. Full coverage sawtooth or V-groove shaped riblets at a height of $100\mu\text{m}$ produced roughly 6% drag reduction. Partial coverage performed best with sawtooth/V-groove shapes of $80\mu\text{m}$ height achieving 4% drag reductions. The optimum full coverage case was the overall best but the benefit was considered offset by the additional application cost.

In Bixler & Bushan (2013), experiments using open channel flow with water, oil and air were able to reduce drag using riblets. On flat plates water channel experiments achieved maximum drag of 6% correlating with oil channel findings. Maximum drag reduction was proven possible using blade riblets at nearly 9% and height/spacing (h/s) ratio of 0.5 and a thickness/spacing (t/s) of 0.04. Results overall indicate that staggered, segmented trapezoidal riblets provided less drag reduction than blade riblets but were able to achieve this over a greater range of configurations.

Airfoil experiments by the American Institute of Aeronautics and Astronautics (Bixler & Bushan 2013, 4518) conducted wind tunnel testing on a DU 96-W-180 wind turbine aerofoil and an NACA 0012 symmetrical aerofoil by utilizing 3M vinyl manufactured riblet sheets. Drag was reduced by around 2% on the DU 96-W-180 aerofoil and up to 7% on the NACA 0012, as long as riblet heights and Reynold's numbers remained low. Angle of attack was also optimum around $\alpha = 6^\circ$ (See Figures 2.9 (a) & (b)).

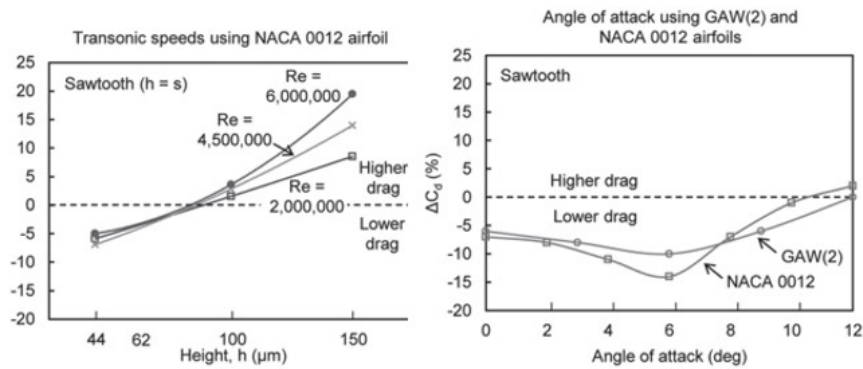


Figure 2.9: (a) Air flow in wind tunnel with riblets. (b) Angle of attack using NACA0012 aerofoils. (Adapted from (Bixler & Bushan 2013, 4518)).

2.5.2 Proposed Non-uniform Riblet Designs

There has been significant research into the application of riblets for improving fluid dynamics over aerofoils. Many studies have experimented with varying the geometry relating to height, spacing, shape and coverage, however, the same geometrical features are always used to cover the surface of the aerofoil whether in entirety, as a portion or simply upper versus lower. It becomes evident that a gap exists where no existing study could be found that modifies riblet geometries from aft to rear along the chord line, specifically to address the variation in shear stress and kinetic energy distributions.

Although these properties will fluctuate with varying angles of attack, wind velocity and turbulent effects, this study hopes to discover under controlled conditions if there would be benefit in modifying several parameters relating to riblet height and spacing along the length of the aerofoil. One such example will include using a blade riblet height of $0.25\mu\text{m}$ towards the fore and increasing to $100\mu\text{m}$ at the aft where the vortices are more developed and the boundary layer thicker, requiring a higher protrusion height to prevent cross-stream flow velocity as noted in Dean & Bhushan (2010).

2.5.3 Shear Stress and Kinetic Energy Distribution Along an Aerofoil

In Figure 2.10 below, studies by Lee & Jang (2005) demonstrate that the Reynolds shear stress distribution along the chord length varies, with the greatest concentration observed where the greatest lift occurs along the aerofoil. The stress concentration reduces as the flow moves aft (greater x/c). Figure 2.11 indicates the same variation for turbulent kinetic

energy distribution along the surface. Again these encourage the need for research into a non-uniform riblet design approach.

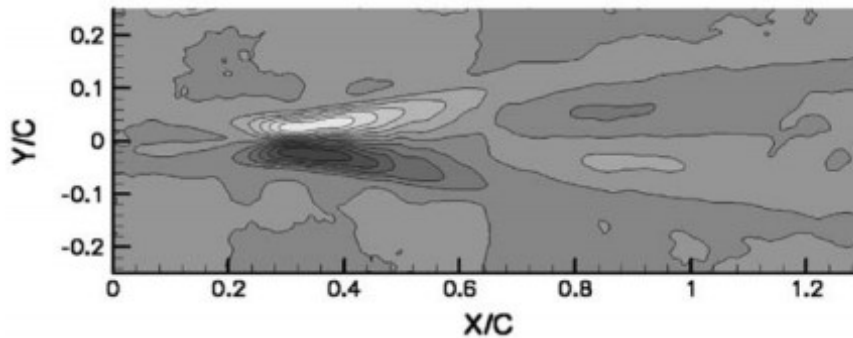


Figure 2.10: Variation of Reynolds shear stress distribution ($Re=1.54 \times 10^4$) (Lee & Jang 2005, 668)

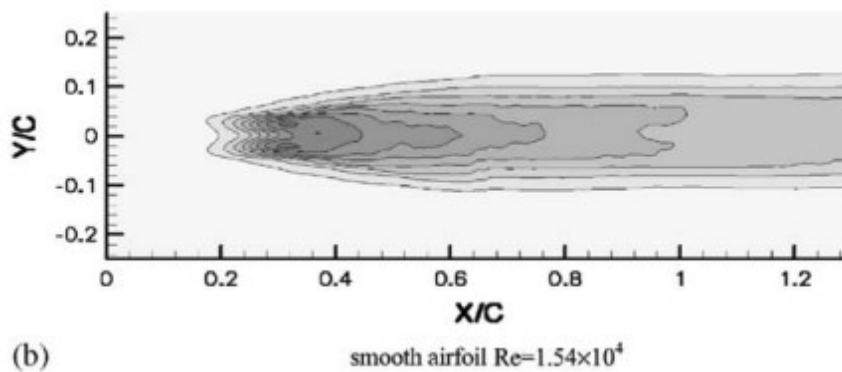


Figure 2.11: Variation of turbulent kinetic energy distribution ($Re=1.54 \times 10^4$) (Lee & Jang 2005, 667).

This study builds upon previous studies and attempt to mimic as much as possible of proven methodologies for riblet analysis, in particular those Bixler & Bushan (2013). The project will show whether varying riblet geometry along an aerofoil rather than keeping uniform features and distribution provides superior flow characteristics. This project will help to increase the body of knowledge surrounding the use of riblets for improving airflow characteristics over wind turbines and further improve broader ranging implications of wind farm wake characteristics.

2.5.4 Environmental and social impact

The environmental and social impact of this study is broad ranging. The major implication stems from increasing wind energy cost effectiveness and therefore desirability. The result is an increasing use of wind technology and/or increased density of wind turbines in farms. Twidell & Weir (2015) covers a comprehensive list of current social, economic and environmental impacts. These have been modified to fit this project's proposed research outcome of reducing drag and increasing energy capture:

- “The nation benefits from the use of wind power because electricity from wind power mitigates the emissions and costs of fossil fuels, and therefore decreases impact causing climate change” (Twidell & Weir 2015, 316)
- Improved efficiency promotes desirability for wind farms, increasing employment opportunities and increasing national energy security benefits
- Wind turbines are often obscured by hills, buildings and trees. Reductions in wake mean potential to increase density. This may reduce the visual impact if sites are half the size, however, if the same land use is doubled in density then this may be a negative impact. Offshore farms would be least impacted due to their isolation
- Audible noise from turbines is expected to be $< 40dBa$ at 250m. If the project yields turbines producing the same output at slower wind speeds, noise will be reduced. If farm density is increased and land required decreased the sound will be further isolated within a smaller zone. If, however, density increased and land use remains the same then sound would increase negatively impacting the area
- In agriculture horses and cattle become accustomed to the noise and land for crops continues unaffected outside of the 1-2% used by the tower bases. Greater density would increase this only marginally
- In general land use may be impacted in two opposing ways. If greater efficiency and less wake increases density, then land use may be halved for the same output. Alternatively, if density is increased on already existing land use then the impact would increase. This is likely to be minor if at all
- TV, microwave, radar may be affected by an increased wind farm growth but only on a minor scale

- Power grids may require upgrading if more power is being generated from existing areas
- Electricity as a whole can be offered cheaper and the community supported through jobs and renewable offsets,

2.6 Literature Review for Further Research

2.6.1 3D Prototype Printing

3D printing provides rapid and cheap prototyping useful for experimentation. The advantages and disadvantages of 3D printing for wind-tunnel models investigated by Kroll & Artzi (2011) included lowering costs through sacrificing internal material which in typical machining processes generally increases complexity and cost, improved time efficiency through complete automation, improved geometrical complexity, reduced weight allowing more sensitive force balance in tests, high accuracy better than 0.1mm and smooth surface finish comparable to fine machining. The disadvantages are reduced strength, stiffness, durability, stability and size limitations based on the 3D printing machine. Reducing these properties can cause aerofoils to behave differently in wind tunnel testing if aerofoils are not printed with enough rigidity to withstand friction and lift forces. This can be overcome by printing with more solidity or by adding internal supports structures but costs rise.

An evaluation of printing techniques by Olasek & Wiklak (2014) compared Multi-Jet Modelling (MJM), Selective Laser Sintering (SLS) and Fused Deposition Modelling (FDM) for 3D printed aerofoils in wind tunnel testing. Ultra-high definition MJM was able to achieve surface roughness comparable to aluminium aerofoil manufactured by electrical discharge machining ($0.84\mu\text{m}$) SLS was comparable to subtractive machining whilst FDM incurred a very high roughness value.

A study by Tyler et al. (2005) included the use of stereolithography (SLA), a technique in which a photo-curable liquid resin is successively hardened, layer by layer using UV/laser light. Current products on the market are able to achieve resolutions as fine as 5 micrometers. Due to its very high resolution and smooth surface finish, stereolithography (SLA) printing would be recommended for prototype research to provide more accurate

boundary layer conditions. Chord lengths of the aerofoil could be printed in prototypes of 175mm is often the limitations in dimensions for most SLA machines on the market. Alternatives options have been investigated below as way of risk mitigation:

- Alternative 1: Aerofoils could be printed using PLA and sanded smooth before re-printing the riblets onto the smoothed surfaces.
- Alternative 2*: Aerofoils could be printed using PLA and post-processing a smooth finish in an acetone vapour bath thereby also smoothing the riblet walls. Research by Valerga et al. (2019) into the impact of chemical post-processing in fused deposition modelling using PLA, found an improvement in roughness of up to 97%. Beniak et al. (2018) specifically tested roughness values for PLA in an acetone vapour bath with roughness values averaging 0.4μ , equivalent to an ISO grade of N12 as per ISO 1302:2002 (ISO 2002) and considered a very fine finish.
- Alternative 3*: Aerofoils could be printed using ABS (Acrylonitrile Butadiene Styrene) and processed in an acetone vapour-bath as in alternative 2. Research by Garg et al. (2016) smoothed ABS samples to $0.31\text{-}0.62\mu$ producing a polished surface texture which is supported by common practices amongst 3D printing enthusiasts.

* In methods 2 and 3, initial test samples should be printed with riblets prior to acetone vapour smoothing so as to also smooth the riblet walls. Adjustments can be made to the methodology if the organic solvent has too great of an effect on the riblets.

2.6.2 Wind Tunnel Considerations

There are inherent limitations in wind tunnel testing a scale model. Petterson (2006) explains that lower Reynolds numbers in wind tunnel testing thins the turbulent boundary layer and shifts the transition point aft on the aerofoil. Thinning the boundary layer may reduce the effectiveness of riblets, but only after a certain threshold as they are designed to remain just within the boundary layer. Other considerations are string-support interference effects and wall interference effects.

Typical Reynolds numbers for wind turbine blades range between 1×10^6 to 1×10^7 as in Figure 15. This is supported by studies conducted by Abbot & Doenhoff (1959) which

indicated reliable values in experiments at $Re=3 \times 10^6$, 300K, $\rho=1.225kg/m^3$ and viscosity $\mu=1.7894 \times 10^{-5}kg/ms$ (Abbot & Doenhoff 1959).

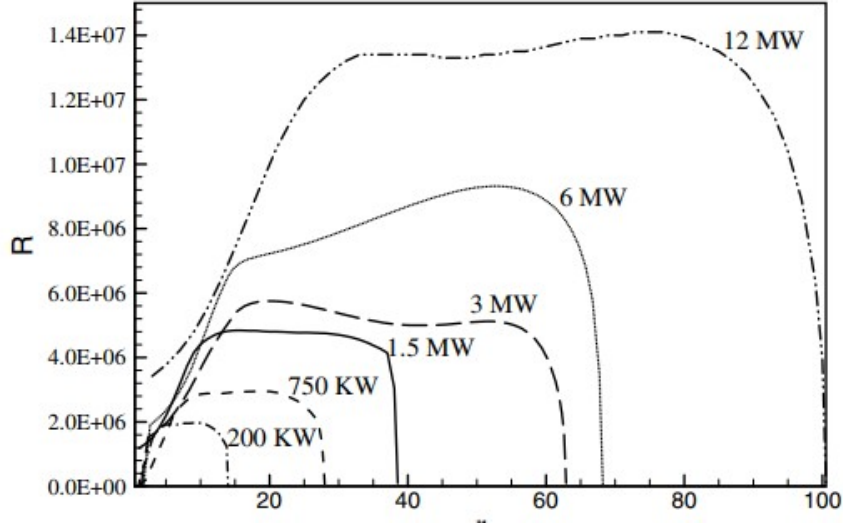


Figure 2.12: Distribution of Reynolds numbers with length of blade for 6 common wind turbines(Ge et al. 2016, 2)

The Reynolds number is represented by:

$$Re = \frac{\rho U_c L}{\mu} \quad (2.5)$$

where ρ =density, U_c is the relative velocity of airflow over the aerofoil, l is the chord length and μ is the dynamic viscosity. To double check the validity of the Reynolds numbers for testing, it is useful to look at a wind turbine example currently in use - the Siemens Gamesa SG 2.7-129 - which saw 163 new installations in North America in 2019 (Siemens Gamesa 2019). According to product information from Siemens Gamesa Renewable Energy, the 2.75MW SG 2.7-129 operates at 12.5 rpm with a diameter of 129m. The velocity of the blade tips is therefore:

$$v = \omega r = \left(\frac{12.5 \times 2\pi}{60} \right) \times \frac{129}{2} = 84.43m/s \quad (2.6)$$

This represents the tip speed at operating conditions and would be approximately 42m/s mid-blade, reducing linearly towards the hub. Typical root chord lengths are around 4m reducing towards the tip according to blade design formulas such as the Betz method (Schubel & Crossley 2012, 3431). Detailed propriety design information for the SG 2.7-129 is diffi-

cult to attain but a safe assumption mid-blade would be a chord length of approximately half i.e. 2m. Thus, the Reynolds number can be estimated from equation (11) to be:

$$\frac{(1.225kg.m^{-3} \times 42ms^{-1} \times 2m)}{1.7894 \times 10^{-5}kg.ms} = 5.75 \times 10^6 \quad (2.7)$$

At 2.75MW, the SG 2.7-129 Reynolds number is in good agreeance with Figure 15. However, due to manufacturing the aerofoils for this project will have a chord length of 175mm. Using the parameters given by Abbot & Doenhoff (1959) the required relative velocity of airflow over the proposed 3D printed prototype becomes:

$$U_c = \frac{3 \times 10^6 \times 1.7894 \times 10^{-5}kg.ms^{-1}}{1.225kg.m^{-3} \times 0.20m} = 250m/s \quad (2.8)$$

If this is not practicable in the facilities available for further research then wind tunnel speeds may be tested at typical undisturbed wind speeds of 5,10,15 and 20 m/s. This concurs with operating conditions of the SG 2.7-129 of 5.5m/s-9.5 m/s and typical safety cutout speeds of around 20 m/s. As an example, at 20 m/s, the Reynolds number for this study using values of air at 250°C and 1 atm from Çengel & Ghajar (2015), will be in the vicinity of:

$$\frac{1.184kg.m^{-3} \times (5 \text{ to } 20)ms^{-1} \times 0.175m}{1.849 \times 10^{-5}kg.ms} = 5.60 \times 10^4 \text{ to } 2.24 \times 10^5 \quad (2.9)$$

Although this is much lower than real world application, this range is commonly used for small-scale testing, as supported by Caram & Ahmed (1991) whom tested similarly sized (76-152µm) 3M riblets applied at 10% of the chord and at $Re = 2.5 \times 10^5$, resulting in a net reduction in drag of up to 13.3%. Jha et al. (2018) investigated the effects of Reynolds numbers on the NACA 0012 aerofoils at various angles of attack using Reynolds numbers closer to this value (Reynolds numbers of 2.21×10^5 and 2.81×10^5 were compared). The results indicated that flow remained attached up until an angle of attack of 13 deg and that an increase in Reynolds number increased the coefficient of lift due to the viscous effects dominating inertial forces at lower numbers and causing higher drag. Therefore, the effect of the riblets may be more pronounced in reducing drag at these values. This suggests that their effectiveness in wind turbine blades is likely to be more pronounced at startup wind speeds and become less significant as inertia forces dominate viscous forces

and potential vortex generation diminishes at typical operating speeds. This meets the objective of the study by improving wind turbine energy extraction during startup and at lower wind speeds.

Chapter 3

Research Methodology

3.1 Project Development

3.1.1 Procedure for Modelling and Simulations

The first step is to model the geometry of an NACA 0012 aerofoil, defined by Chang et al. (1995) by the following equation:

$$y = \frac{t}{0.2}(0.2969\sqrt{x} - 0.126x - 0.3516x^2 + 0.2843x^3 - 0.1015x^4) \quad (3.1)$$

where (t) is the maximum thickness expressed as a fraction of the chord which is of unit length. The function y can then be rewritten in terms of the following four shape functions:

$$g_1(x) = \sqrt{x} - x \quad (3.2)$$

$$g_2(x) = x(1 - x) \quad (3.3)$$

$$g_3(x) = x^2(1 - x) \quad (3.4)$$

$$g_4(x) = x^3(1 - x) \quad (3.5)$$

where x is the closed unit interval $[0,1]$. These represent the 4 digits (0012) of the NACA code and can be simplified as a symmetrical aerofoil that is 12% thick as it is long (Abbot & Doenhoff 1959). Mesh scale and geometries will be processed by the software with consideration to time efficiency/computing capability versus accuracy. The mesh will

undergo several refinement stages until optimum. Software analysis will be run at zero degrees angle of attack $\alpha = 0$ with respect to the chordline due to time limitations imposed for this research and exacerbated by computing power restraints, thus the work will focus on gaining in depth and valuable data in one specific baseline, availing additional angles of attack to further research efforts. It should be mentioned that there is an NACA 0012 angle of attack limitation of approximately 13° as noted in Jha et al. (2018). This is supported by Viswanath (2002) finding that higher angles of attack do not necessarily yield better results, thought to be attributed to boundary layer separation.

Fluid velocities will be adjusted between 5-20 m/s in 5 m/s increments and then in 10 m/s increments up to 90 m/s which is closer to NASA values and in line with many wind turbine tip speeds where the tangential speed of the blade is far greater than the oncoming undisturbed wind speed. This represents the majority of the range within which a typical wind turbine operates. At each stage meshing may need to be adjusted depending on movement of the transition point. The aerofoils will be re-modelled several times with the addition of riblets of varying geometry to both the upper and lower surfaces. In practice, manufacturing techniques and requirements for durability regard sawtooth riblets as superior, however, for this study and in reducing complexity of meshing, blade riblets will be chosen. Riblet heights will vary from 25-100 μm from forward to aft and vice versa, as shown in Figure 3.1:

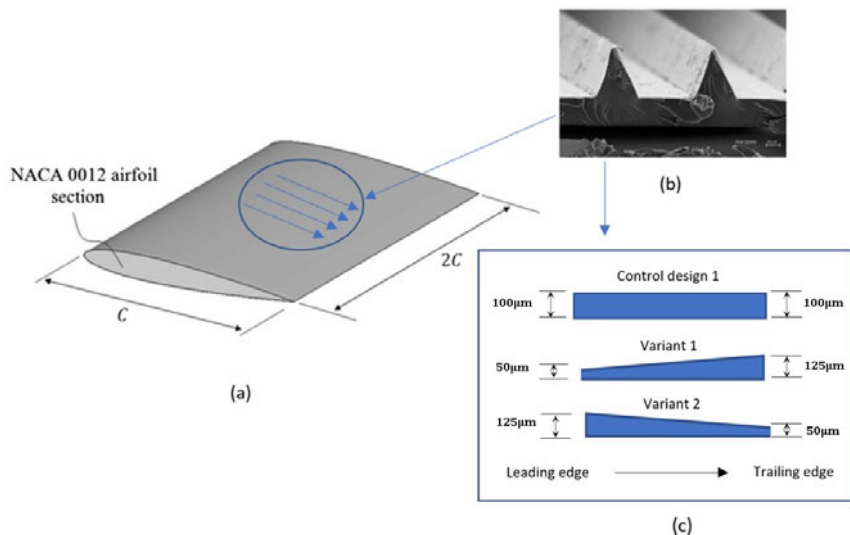


Figure 3.1: (a) NACA 0012 aerofoil section (adapted from (Yousefi & Saleh 2015, 1483)). (b) 3M riblet film under scanning electron microscope (Sidhu et al. 2016, 7694). (c) Proposed variants to riblet geometry for this study.

Lateral separation of riblets is based on experimental findings from Bixler & Bushan

(2013) which is a height to spacing ratio of 0.5. As riblets increase in height along the chord line, the spacing will also need to increase to maintain this ratio. Therefore, riblets will increase in set increments from $50\mu\text{m} < 75\mu\text{m} < 100\mu\text{m} < 125\mu\text{m}$. This allows the spacing to increase similarly from $100\mu\text{m} < 150\mu\text{m} < 200\mu\text{m} < 250\mu\text{m}$ as shown in Figure 3.2 below. The inverse of this would apply to variants of height in the opposite direction. The starting location will match Bixler & Bushan (2013) beginning 12% aft of the leading edge and continuing for 96% of the chord. Results from simulation will be analysed to determine the effects on the boundary layer.

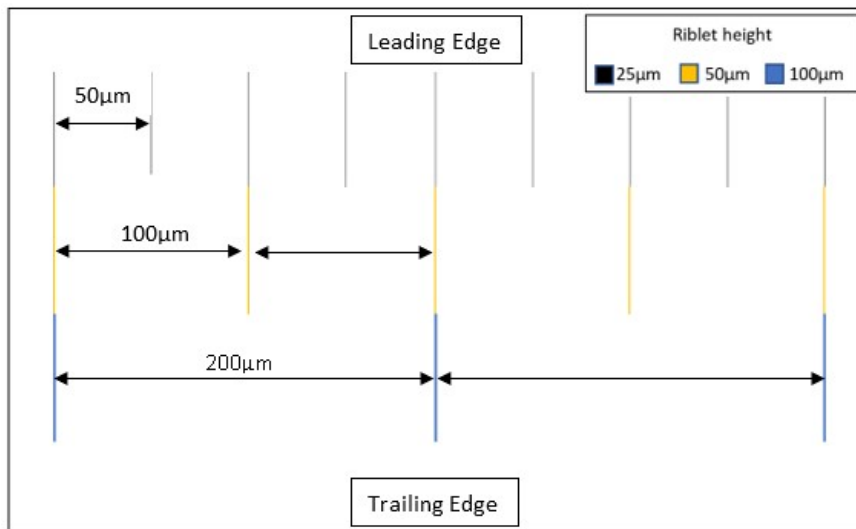


Figure 3.2: Riblet spacing to maintain height to spacing ratio of 0.5.

3.1.2 Limitations

Several limitations exist to this project. They are:

- Flow in the blade tip and root region is three-dimensional due to centrifugal and Coriolis forces the flow in the boundary layer at the root is in spanwise direction, while flow outside is chordwise. The relevance of two-dimensional data for wind turbine performance prediction is very limited. Complex CFD models based on Reynolds-averaged Navier-Stokes (RANS) equations may enhance accuracy but limitations remain in meshing capability and the need for an artificial compressibility term in the equations to account for the role of pressure which is not satisfied in every instant. Therefore, two-dimensional computations or measurements are able to be corrected for three-dimensional effects. The most significant effect occurs as

rotational effects limit the growth of the boundary layer which increases lift in rotating blades hence the lift effect is diminished in two-dimensional analysis (Vermeer et al. 2003, 481). This highlights the difficulty in pursuing a holistic solution to blade design and is beyond the complexity of this project, which will focus on 3D models limited to two-dimensional flow characteristics as a validation and precursor of worthiness for conducting further in-depth studies.

- Wind turbines are designed to stall, limiting speeds and reducing power efficiencies lost to mechanical braking. Therefore, at maximum operating speeds they will inherently create turbulence from the boundary layer separation following stall conditions. However, in all other operation i.e. lower wind speeds, improved coefficient of lift to coefficient of drag ratios may be achieved increasing energy capture. Furthermore, wind turbines in the downstream turbulent wake fields will also perform better under these conditions.
- Modelling software is limited in its application as this field of study is yet to be fully understood and so may not account for the complex flow outcomes seen in experimental data, particularly relating to vortex generation and control,

3.1.3 Expected outcomes and benefits

This project will improve understanding of airflow over riblets on an aerofoil. It seeks to enhance pre-existing knowledge and concepts of how riblets elevate, pin and separate vortices from entanglement at the transition zone of the boundary layer. The findings of this study will open the way to future research projects in the field of fluid dynamics. The expected outcomes of this project include:

- Increased understanding of boundary layer characteristics in aerofoils, in particular the mitigation of turbulent vortex generation and/or improved methods for control of vortices
- Increased behavioural understanding of the NACA 0012 aerofoil with riblets, under several controlled wind conditions
- Validation of the concept of applying riblets to wind turbine blades as a means of reducing drag and improving power generation at lower wind speeds

- Increased appreciation of the validity of computational fluid dynamics for solving complex fluid problems,

These outcomes will provide strong grounds for future research into improving riblet design and may see their implementation into hydro and wind energy sectors. There is potential that wind turbines can be expanded to regions of lower wind speeds. From literature it would not be unreasonable to consider regions with average wind velocities of 6% less than current minimum standards becoming newly viable for energy capture, dependent upon the findings of this study. This also has the potential to improve wind farm clustering, increasing energy output density. Any improvements in renewable energy may lessen the use of fossil fuels reducing the carbon footprint and human induced global warming effects. The fluid mechanics in this sector is also applicable to hydropower and aviation and may prompt further research in these fields.

3.2 Project Planning

3.2.1 Resource Requirements

Resource requirements are recorded in Table 3.1. Research hours invested can exceed 800 hours over the duration of the research spanning late 2019 to late 2020. This time accounts for the project activities outlined in Table 3.2 and the project schedule in Table 3.3 and includes modelling and analysis, prototyping, experimenting, analysis and interpretation of results and preparing the dissertation. This does not factor in the additional time required by TUSQ staff and supervisors in reviewing dissertation material and liaising with the researcher throughout the project.

Table 3.1: Resource requirements

Item	Quantities	Source	Cost	Comment
PC with Microsoft Windows	1	Personal	-	Already owned
PC Memory upgrade	1	Personal	660	Required for simulations
PC Monitor upgrade	1	Personal	330	Required for visual space and clarity
SOLIDWORKS Flow Simulation	1	Business	-	Already acquired
Microsoft Office	1	Personal	-	Already acquired
LaTeX	1	Online	-	Already acquired
Sundry items	As required	Personal	100	Printing research items, draft and final dissertation

3.2.2 Project Schedule

This project is designed to take place in 2020 within the Semester 1 and 2 timeframes for ENG4111 (Research Project Part 1) and ENG4112 (Research Project 2), including ENG4903 (Professional Practice 2). The key milestones in the project schedule are further detailed in Table 3.3 below:

3.2.3 Risk Assessment

A risk assessment has been conducted using a template whereby likelihood and severity of occurrence form a matrix of risks from low to extreme (Table 3.4). Results are shown in Table 3.5 overleaf:

3.2.4 Quality Assurance Plan

To ensure the quality of this research the following checks and measures will be incorporated:

- Software versions will be verified to ensure the latest versions are utilised
- All SOLIDWORKS Flow Simulation software models will be compared to known values in previous studies as well as comparing to NASA's CFD database
- Results will be verified against two control specimens. The primary control will be a smooth aerofoil. The second control will be an aerofoil with $100\mu m$ uniform riblets for comparison to previous studies of the same specification
- The same methodology will be strictly adhered to across all models

Prior to submitting the final dissertation, draft submissions will be provided to USQ for review and feedback. Throughout the course of the project communication and regular reviews will take place with the university assigned supervisor at each critical phase of the project. Advice and feedback will be incorporated into the project before proceeding at each step towards creating the final dissertation.

Table 3.2: Project Task Descriptions

Phase 1 1. Project Preparation Phase	
1A	Project commencement approval - Obtain official approval from The University of Southern Queensland to commence research
1B	Review project books and literature review material - read and understand requirements for assessment
1C	Resource acquisition - Install SOLIDWORKS Flow Simulation, LaTeX and related software components
1D	Revise software - Revise use of SOLIDWORKS, Airfoil Tools
1E	Travel booking for Professional Practice 2 - Book annual leave and flights to Australia
Phase 2 Benchmark Modelling/Calibration Phase	
2A	Model standard NACA 0012 aerofoil - Use Autodesk Inventor to model step files of aerofoil designs
2B	Mesh standard NACA 0012 aerofoil - Use SOLIDWORKS Flow Simulation to create and refine mesh iteratively before final simulation
2C	Analyse new designs - Use SOLIDWORKS Flow Simulation to analyse and record results of aerofoils at the selected windspeeds and angles of attack
2D	Produce/record data - Cl, Cd, AOA and x/c pressure data - Record data in appropriate tables for use in analysis
2E	Plot data - Create plots for Cl vs Cd, AOA and x/c pressure data
2F	Analyse data - Analyse and validate results against NASA et al.
Phase 3 Modelling and Simulation Phase 1 (NACA 0012 Aerofoil)	
3A	Model proposed variants - model several NACA 0012 aerofoils with riblet variations
3B	Mesh new designs - Use SOLIDWORKS Flow Simulation to create and refine mesh iteratively before final simulation
3C	Analyse new designs - Use SolidWorks to analyse and record results of aerofoils at the selected windspeeds and angles of attack
3D	Produce/record data - Cl, Cd, AOA and x/c pressure data - Record data in appropriate tables for use in analysis
3E	Plot data - Create plots for Cl vs Cd, AOA and x/c data
Phase 4 Modelling and Simulation Phase 2 (Wind Turbine Blade)	
4A	Model S-802 Wind Turbine Blade - repeat methodology from NACA0012 with S-802 design
4B	Mesh new designs - repeat methodology from NACA0012 with S-802 design
4C	Analyse new designs - use SolidWorks to analyse and record results of aerofoils at the selected windspeeds and angles of attack
4D	Produce/record data - Cl, Cd, AOA and x/c pressure data - Record data in appropriate tables for use in analysis
4E	Plot data - Create plots for Cl vs Cd, AOA and x/c data
Phase 5 Data Analysis Phases	
5A	Interpret and discuss results for NACA0012 research designs - Evaluate design effectiveness and give detailed reasoning for results
5B	Interpret and discuss results for S-802 Wind Turbine Blade application - Evaluate design effectiveness and give detailed reasoning for results
5C	Conclusion and further work - Conclude findings and discuss the avenues for further research possibilities
Phase 6 Write-up and Presentation of Results Phase	
6A	Prepare draft dissertation - Complete draft for submission by assessment deadline
6B	Present preliminary results at Professional Practice 2 - complete practical phase
6C	Complete dissertation and submit - complete Project2020 final assessment

Table 3.4: Risk Assessment Matrix

RISK SEVERITY KEY		RISK LIKELIHOOD KEY		RISK LEVEL KEY		ACCEPTABLE TO PROCEED? KEY	
ACCEPTABLE		IMPROBABLE		LOW		YES	
TOLERABLE		POSSIBLE		MEDIUM		NO	
UNDESIRABLE		PROBABLE		HIGH			
INTOLERABLE				EXTREME			

RISK RATING KEY	LOW	MEDIUM	HIGH	EXTREME
	0 – ACCEPTABLE OK TO PROCEED	1 – ALARP (as low as reasonably practicable) TAKE MITIGATION EFFORTS	2 – GENERALLY UNACCEPTABLE SEEK SUPPORT	3 – INTOLERABLE PLACE EVENT ON HOLD

	SEVERITY			
	ACCEPTABLE	TOLERABLE	UNDESIRABLE	INTOLERABLE
	LITTLE TO NO EFFECT ON EVENT	EFFECTS ARE FELT, BUT NOT CRITICAL TO OUTCOME	SERIOUS IMPACT TO THE COURSE OF ACTION AND OUTCOME	COULD RESULT IN DISASTER
LIKELIHOOD				
IMPROBABLE RISK IS UNLIKELY TO OCCUR	LOW - 1 -	MEDIUM - 4 -	MEDIUM - 6 -	HIGH - 10 -
POSSIBLE RISK WILL LIKELY OCCUR	LOW - 2 -	MEDIUM - 5 -	HIGH - 8 -	EXTREME - 11 -
PROBABLE RISK WILL OCCUR	MEDIUM - 3 -	HIGH - 7 -	HIGH - 9 -	EXTREME - 12 -

Table 3.5: Risk Assessment

PHASE	PRE-MITIGATION				MITIGATIONS / WARNINGS / REMEDIES	POST-MITIGATION			
	RISK	RISK SEVERITY	RISK LIKELIHOOD	RISK LEVEL		RISK SEVERITY	RISK LIKELIHOOD	RISK LEVEL	PROCEED?
1. Project Preparation Phase									
1A. Project commencement approval	Project not approved	INTOLERABLE	POSSIBLE	EXTREME	Commence discussions and application for approval early. Have alternative project idea	TOLERABLE	POSSIBLE	MEDIUM	YES
1B. Review project books and literature review material	Falling behind early in project	UNDESIRABLE	POSSIBLE	HIGH	Begin prior to semester start	ACCEPTABLE	IMPROBABLE	LOW	YES
1C. Resource acquisition	Resources unavailable	INTOLERABLE	PROBABLE	EXTREME	Majority of resources already acquired	ACCEPTABLE	IMPROBABLE	LOW	YES
1D. Revise software	Unable to learn software	INTOLERABLE	PROBABLE	EXTREME	Begin tutorials prior to semester starting	TOLERABLE	POSSIBLE	MEDIUM	YES
1E. Travel booking for Professional Practice 2	Flights unavailable, cancelled or leave unapproved	INTOLERABLE	PROBABLE	EXTREME	Book flights early with insurance for secondary flights. Apply for leave early.	ACCEPTABLE	IMPROBABLE	LOW	YES
2. Benchmark Modelling/Calibration Phase									
2A. Model standard NACA 0012 aerofoil	Software fails to model or unable to model confidently	INTOLERABLE	IMPROBABLE	HIGH	Rely on previous experience and early access in 2019 plus the wealth of online resources and educational material	TOLERABLE	IMPROBABLE	MEDIUM	YES
2B. Mesh standard NACA 0012 aerofoil	Software fails to model or unable to mesh confidently	INTOLERABLE	IMPROBABLE	HIGH	Rely on previous experience and early access in 2019 plus the wealth of online resources and educational material	TOLERABLE	IMPROBABLE	MEDIUM	YES
2C. Analyse new designs	Unable to learn CFD analysis	INTOLERABLE	IMPROBABLE	HIGH	Rely on previous experience and early access in 2019 plus the wealth of online resources and educational material	TOLERABLE	IMPROBABLE	MEDIUM	YES
2D. Produce/record data	Unable to produce data	INTOLERABLE	IMPROBABLE	HIGH	Trial basic data production prior to semester start and topic allocation	TOLERABLE	IMPROBABLE	MEDIUM	YES
2E. Plot data	Data is not sufficient to produce plots	UNDESIRABLE	IMPROBABLE	MEDIUM	Trial plotting basic data following step 2D	TOLERABLE	IMPROBABLE	MEDIUM	YES
2F. Analyse data	No models are appropriate	UNDESIRABLE	POSSIBLE	HIGH	Testing will continue but results of dissertation are likely to be inconclusive	TOLERABLE	POSSIBLE	MEDIUM	YES
3. Modelling and Simulation Phase 1 (NACA 0012 Aerofoil)									
3A. Model proposed variants	Software fails to model or unable to model confidently	INTOLERABLE	IMPROBABLE	HIGH	Rely on previous experience and early access in 2019 plus the wealth of online resources and educational material	TOLERABLE	IMPROBABLE	MEDIUM	YES
3B. Mesh new designs	Software fails to model or unable to mesh confidently	INTOLERABLE	IMPROBABLE	HIGH	Rely on previous experience and early access in 2019 plus the wealth of online resources and educational material	TOLERABLE	IMPROBABLE	MEDIUM	YES

Table 3.6: Risk Assessment (continued)

3C. Analyse new designs	Unable to learn CFD analysis	INTOLERABLE	IMPROBABLE	HIGH	Rely on previous experience and early access in 2019 plus the wealth of online resources and educational material	TOLERABLE	IMPROBABLE	MEDIUM	YES
3D. Produce/record data	Unable to produce data	INTOLERABLE	IMPROBABLE	HIGH	Trial basic data production prior to semester start and topic allocation	TOLERABLE	IMPROBABLE	MEDIUM	YES
3E. Plot data	Data is not sufficient of produce plots	UNDESIRABLE	IMPROBABLE	MEDIUM	Trial plotting basic data following step 2D	TOLERABLE	IMPROBABLE	MEDIUM	YES
4. Modelling and Simulation Phase 2 (Wind Turbine Blade)									
4A. Model S-802 Wind Turbine Blade	Software fails to model or unable to model confidently	INTOLERABLE	IMPROBABLE	HIGH	Rely on previous experience and early access in 2019 plus the wealth of online resources and educational material	TOLERABLE	IMPROBABLE	MEDIUM	YES
4B. Mesh new design	Software fails to model or unable to mesh confidently	INTOLERABLE	IMPROBABLE	HIGH	Rely on previous experience and early access in 2019 plus the wealth of online resources and educational material	TOLERABLE	IMPROBABLE	MEDIUM	YES
4C. Analyse new design	Unable to learn CFD analysis	INTOLERABLE	IMPROBABLE	HIGH	Rely on previous experience and early access in 2019 plus the wealth of online resources and educational material	TOLERABLE	IMPROBABLE	MEDIUM	YES
4D. Produce/record data	Unable to produce data	INTOLERABLE	IMPROBABLE	HIGH	Trial basic data production prior to semester start and topic allocation	TOLERABLE	IMPROBABLE	MEDIUM	YES
4E. Plot data	Data is not sufficient of produce plots	UNDESIRABLE	IMPROBABLE	MEDIUM	Trial plotting basic data following step 2D	TOLERABLE	IMPROBABLE	MEDIUM	YES
5. Data Analysis Phases									
5A. Interpret and discuss results for NACA0012 research designs	Unable to interpret due to poor data or inconsistent outcomes	INTOLERABLE	IMPROBABLE	HIGH	If data analysis is insufficient liaise with supervisor and provide evidence of why and attempt to resolve in timely manner	ACCEPTABLE	IMPROBABLE	LOW	YES
5B. Interpret and discuss results for S-802 Wind Turbine Blade application	Unable to create graphs (possible software issue)	INTOLERABLE	IMPROBABLE	HIGH	Seek alternate computer or software	ACCEPTABLE	IMPROBABLE	LOW	YES
5C. Conclusion and further work	Results are unusable or show no useful information	INTOLERABLE	IMPROBABLE	HIGH	Complete dissertation but justify poor outcome, seek the course and how this might have been avoided in future research	TOLERABLE	IMPROBABLE	MEDIUM	YES
6. Write-up and Presentation of Results Phase									
6A. Prepare draft dissertation	Draft dissertation is lost	INTOLERABLE	IMPROBABLE	HIGH	Maintain multiple backup copies on PC and via email. Submission points for supervisor review will also provide redundancy	ACCEPTABLE	IMPROBABLE	LOW	YES
6B. Present preliminary results at Professional Practice 2	Unable to attend due to flights, leave or sickness	INTOLERABLE	IMPROBABLE	HIGH	Follow contingency plan as per project schedule	ACCEPTABLE	IMPROBABLE	LOW	YES
6C. Complete dissertation and submit	Dissertation is lost or incomplete at deadline	INTOLERABLE	IMPROBABLE	HIGH	Seek extension and maintain backup copies as per 6A mitigations above	ACCEPTABLE	IMPROBABLE	LOW	YES

Chapter 4

Numerical Analysis

4.1 Governing Equations

Fluid analysis often relies on the dimensionless expression of inertial to viscous forces known as the Reynolds Number, calculated as:

$$Re = \frac{\rho V L_c}{\mu} \quad (4.1)$$

The flow in this research is considered fully turbulent with almost all initial inlet velocities during simulations resulting in an $Re > 5 \times 10^6$. This is important in deriving governing equations and understanding how these are utilised in computational fluid dynamic software. As such, fully turbulent flow consists of constant fluctuations in velocity and pressure as shown in Figure 4.1:

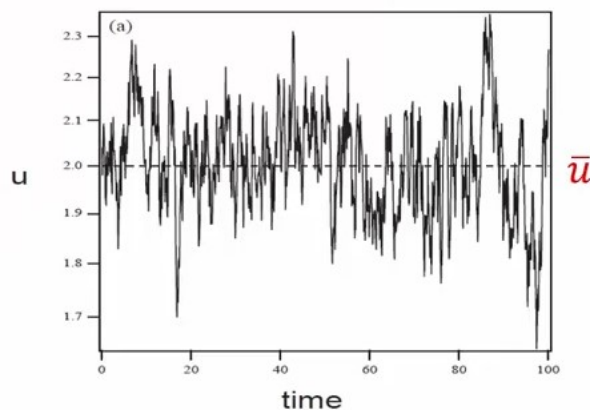


Figure 4.1: Averaged turbulence velocity profile. (Bhaskaran 2019).

This is known as the Reynolds decomposition:

$$u = \bar{u} + u' \quad (4.2)$$

where (u) equals a Reynolds averaged velocity (\bar{u}) and a velocity fluctuation (u').

Taking partial derivatives for the average velocity over time and the average fluctuation during that time leads to the Reynolds-Averaged Continuity Equation:

$$\frac{\partial u}{\partial x} + \frac{\partial v}{\partial y} = 0 \quad (4.3)$$

$$\bar{u} = \bar{u} + \bar{u}' \quad (4.4)$$

$$\frac{\partial \bar{u}}{\partial x} + \frac{\partial \bar{v}}{\partial y} = 0 \quad (4.5)$$

Since continuity is linear for incompressible flows, the Reynolds-Averaged Continuity Equation is the same as the original continuity equation.

Building upon this is the Reynolds-Averaged Navier-Stokes Equations (RANS):

$$\rho \frac{\partial u}{\partial t} + \rho \left(u \frac{\partial u}{\partial x} + v \frac{\partial v}{\partial y} \right) = -\frac{\partial p}{\partial x} + \mu \nabla^2 u \quad (4.6)$$

where the first term represents unsteadiness in the flow, the second is the convection term accounting for convective acceleration due to particle movement, the third is the pressure gradient or net pressure force on an infinitesimal fluid particle and the final operation is the net viscous force.

Finally, normal and shear forces are introduced in the x-direction:

$$\rho \frac{\partial \bar{u}}{\partial t} + \rho \left(\bar{u} \frac{\partial \bar{u}}{\partial x} + \bar{v} \frac{\partial \bar{v}}{\partial y} \right) = -\frac{\partial \bar{p}}{\partial x} + \mu \nabla^2 \bar{u} - \rho \left(\overline{u' \frac{\partial u'}{\partial x}} + \overline{v' \frac{\partial u'}{\partial y}} \right) \quad (4.7)$$

which can be rewritten:

$$\rho \frac{\partial \bar{u}}{\partial t} + \rho \left(\bar{u} \frac{\partial \bar{u}}{\partial x} + \bar{v} \frac{\partial \bar{v}}{\partial y} \right) = -\frac{\partial \bar{p}}{\partial x} + \mu \nabla^2 \bar{u} - \left(\frac{\partial}{\partial x} (-\rho \overline{u'u'}) + \frac{\partial}{\partial y} (-\rho \overline{u'v'}) \right) \quad (4.8)$$

Here the final two terms represent the net turbulent normal stresses and the net turbulent shear stresses on the fluid particles respectively, simplified in Figure 4.2 and Equation (4.9) below:

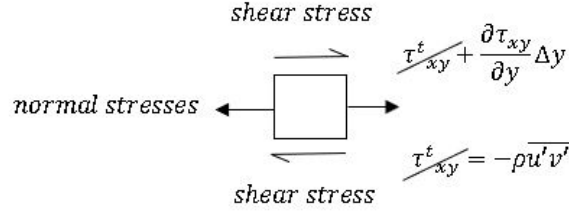


Figure 4.2: Normal and shear stresses on fluid particle

$$\rho \frac{\partial \bar{u}}{\partial t} + \rho \left(\bar{u} \frac{\partial \bar{u}}{\partial x} + \bar{v} \frac{\partial \bar{v}}{\partial y} \right) = -\frac{\partial \bar{p}}{\partial x} + \mu \nabla^2 \bar{u} + \bar{f}_t u r b, x \quad (4.9)$$

4.2 SOLIDWORKS Equations

As described in the SOLIDWORKS Numerical Basis of CAD-Embedded CFD White Paper (Sobachkin & Dumnov 2014), “all CFD software includes a representation of the Navier-Stokes equations, turbulence models and models for physical phenomena”. Traditionally a Boolean subtraction is performed on the CAD model before this inverse solid is given over to a CFD tool for meshing. Basic types of meshes are reviewed in detail in the White Paper including Weatherill & Hassan, 1994, Filipiak, 1996 and Parry & Tatchell, 2008.

For complicated geometries unstructured meshes as shown in Figure 4.3 (a) are constructed using irregular nodes while structured meshes shown in (b) serve lesser complexity geometries. Figure 4.3 (c) represents a combination of the two as required. Usually body-fitted meshes such as these are highly sensitive to the quality of the CAD model as the nodes are first generated at the surface of the model, before being meshed by Delaunay triangulation prior to the remaining space mesh generation, often with tetrahedral elements as seen in Delaunay 1934, Lawson 1977, Watson 1981, Baker 1989 and

Weatherill & Hassan 1994 (Sobachkin & Dumnov 2014). This leads to a requirement for user intervention, over-refinement and excessive small triangles where they may not be significant to the flow simulation and require further remediation. This can be partially attributed to software designed primarily with geometry in mind as opposed to numerical analysis.

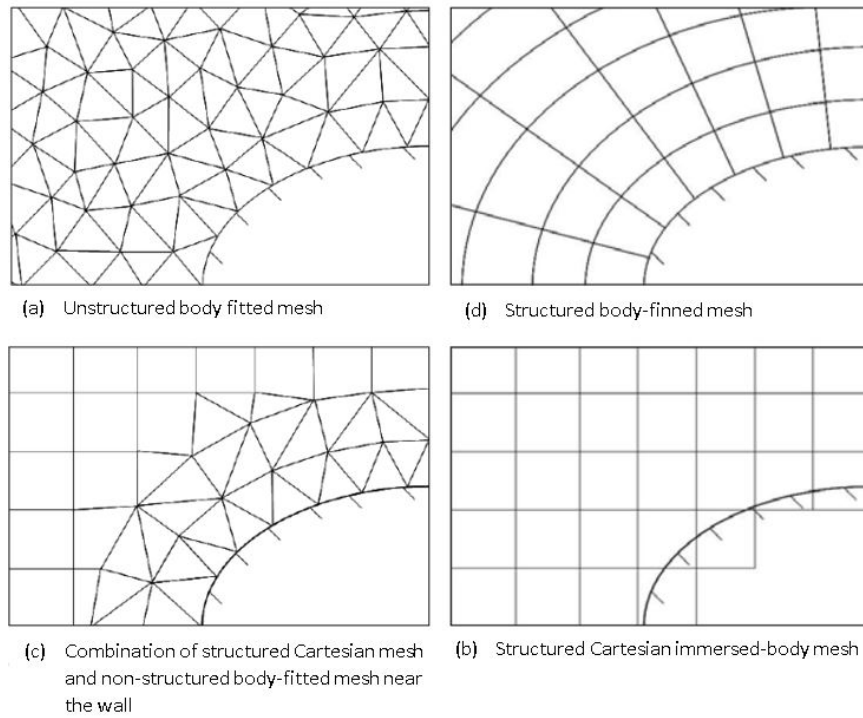


Figure 4.3: Common types of mesh construction for fluid analysis (adapted from (Sobachkin & Dumnov 2014))

SOLIDWORKS Flow Simulation utilises an immersed-body mesh as shown in Figure 4.3 (d) where cells can intersect the boundary between solid and fluid allowing the use of Cartesian-based mesh, defined as a set of external adjacent cuboids along Cartesian coordinates. Cells intersecting both regions are resolved uniquely by dividing the cuboid into control volumes and re-calculating the cell centre. The areas and normal vectors are calculated for the CV faces.

SOLIDWORKS equations involve the Navier-Stokes equations for mass, momentum and energy conservation laws as described in the governing equations and are specifically as follows:

$$\frac{\partial p}{\partial t} + \frac{\partial(\rho u_i)}{\partial x_i} = 0 \quad (4.10)$$

$$\frac{\partial(\rho u_i)}{\partial t} + \frac{\partial}{\partial x_j}(\rho u_i u_j) + \frac{\partial P}{\partial x_i} = \frac{\partial}{\partial x_j}(\tau_{ij} + \tau_{ij}^R) + S_i \quad (4.11)$$

$$\frac{\partial \rho H}{\partial t} + \frac{\partial \rho u_i H}{\partial x_i} = (u_j(\tau_{ij} + \tau_{ij}^R) + q_i) + \frac{\partial p}{\partial t} - \tau_{ij}^R \frac{\partial u_i}{\partial x_j} + \rho \epsilon + S_i u_i + Q_H \quad (4.12)$$

$$H = h + \frac{u^2}{2} \quad (4.13)$$

The equations are supplemented by fluid state equations based on fluid density, viscosity, thermal conductivity, temperature and special models for real gases. When the Reynolds number exceeds a critical value it smoothly transitions to turbulent. SOLIDWORKS Flow Simulation then utilises the k-epsilon model. This model includes damping functions and was first proposed by Lam & Bremhorst (1981) describing laminar, turbulent and transitional flows of homogenous fluids.

$$\frac{\partial \rho k}{\partial t} + \frac{\partial \rho k u_i}{\partial x_i} = \frac{\partial}{\partial x_i} \left(\left(\mu + \frac{u_t}{\sigma_k} \right) \frac{\partial k}{\partial x_i} \right) + \tau_{ij}^R \frac{\partial u_i}{\partial x_j} - \rho \epsilon + \mu_i P_B \quad (4.14)$$

$$\frac{\partial \rho \epsilon}{\partial t} + \frac{\partial \rho \epsilon u_i}{\partial x_i} = \frac{\partial}{\partial x_i} \left(\left(\mu + \frac{u_t}{\sigma_\epsilon} \right) \frac{\partial \epsilon}{\partial x_i} \right) + C_{\epsilon 1} \frac{\epsilon}{k} \left(f_1 \tau_{ij}^R \frac{\partial u_i}{\partial x_j} + C_B \mu_t P_B \right) - f_2 C_{\epsilon 2} \frac{\rho \epsilon^2}{k} \quad (4.15)$$

and;

$$\tau_{ij} = \mu S_{ij} \quad (4.16)$$

$$\tau_{ij}^R = \mu_t S_{ij} - \frac{2}{3} \rho k \delta_{ij} \quad (4.17)$$

$$S_{ij} = \frac{\partial u_i}{\partial x_j} + \frac{\partial u_j}{\partial x_i} - \frac{2}{3} \delta_{ij} \frac{\partial u_k}{\partial x_k} \quad (4.18)$$

$$P_B = -\frac{g_i}{\sigma_B} \frac{1}{\rho} \frac{\partial \rho}{\partial x_i} \quad (4.19)$$

where $C_\mu = 0.09$, $C_{\epsilon 1} = 1.44$, $C_{\epsilon 2} = 1.92$, $\sigma_k = 1$, $\sigma_\epsilon = 1.3$, $\sigma_B = 0.9$, $C_B = 1$ if $P_B > 0$, $C_B = 0$ if $P_B < 0$, the turbulent viscosity is determined from:

$$\mu_t = f_u \cdot \frac{C_\mu \rho k^2}{\epsilon} \quad (4.20)$$

Lam and Bremhorst's damping function f_μ is determined from:

$$f_\mu = \left(1 - e^{-0.025 R_y}\right)^2 \cdot \left(1 + \frac{20.5}{R_t}\right) \quad (4.21)$$

where:

$$R_y = \frac{\rho \sqrt{k} y}{\mu} \quad (4.22)$$

$$R_t = \frac{\rho k^2}{\mu_\epsilon} \quad (4.23)$$

y is the distance from the point to the wall and Lam and Bremhorst's damping functions f_1 and f_2 are determined from:

$$f_1 = 1 + \left(\frac{0.05}{f_\mu}\right)^3 \quad (4.24)$$

$$f_2 = 1 - e^{R_t^2} \quad (4.25)$$

When the Reynolds Number R_y is too small, based on the average velocity fluctuations and distance from the wall, the damping functions f_u , f_1 , f_2 act to decrease turbulent viscosity and energy and increase the turbulence dissipation rate. When the three functions =1 the approach reverts back to the $k - \epsilon$ model.

Heat flux is defined by:

$$q_i = \left(\frac{\mu}{Pr} + \frac{\mu_t}{\sigma_c}\right) \frac{\partial h}{\partial x_i} \quad (4.26)$$

where $i = 1, 2, 3$, $\sigma_c = 0.9$ (Prandtl Number) and h is the thermal enthalpy

In order to calculate the near-wall cells using a Cartesian immersed-body mesh, the program utilises a novel and original Two-Scale Wall Function (2SWF) for coupling high gradient boundary layers with the bulk flow (Sobachkin & Dumnov 2014). The boundary layer is resolved in the three cases below and as represented in Figure 4.4:

1. A “thin boundary layer treatment that is used when the number of cells across the boundary layer is not enough for direct, or even simplified, determination of the flow and thermal profiles; and
2. A “thick” boundary layer approach when the number of cells across the boundary layer exceeds that required to accurately resolve the boundary layer.
3. In intermediate cases, a compilation of the two above approaches is used, ensuring a smooth transition between the two models as the mesh is refined, or as the boundary layer thickens along a surface.

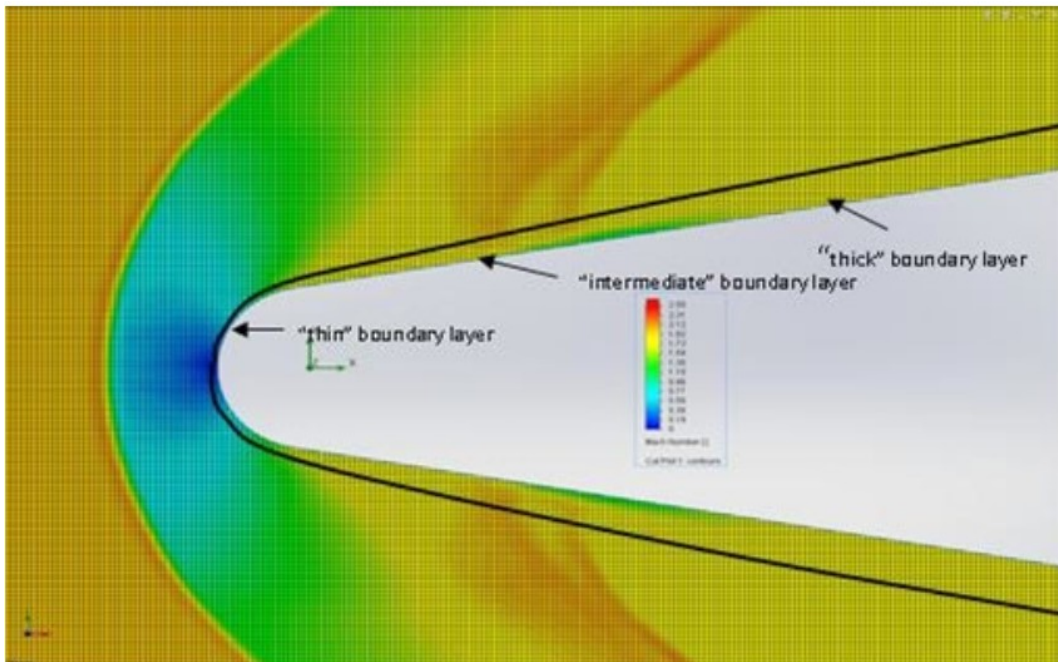


Figure 4.4: Mach Number flow field with "thin", intermediate" and "thick" viscous boundary layer (Sobachkin & Dumnov 2014)

4.2.1 Thin-Boundary-Layer approach

The Prandtl boundary layer equations already integrated along the normal to the wall from 0 to the boundary layer thickness σ are solved along fluid streamlines covering the walls. If laminar successive approximations are made using Shvets trial functions technology (Ginzburg 1970). If turbulent or transitional then the Van Dreist hypothesis about mixing length in turbulent boundary layers is used (Van Dreist 1956). From the boundary layer calculation, the boundary layer thickness σ , wall shear stress τ_w^e and heat flux q_w^e are used as the boundary conditions in the Navier-Stokes equations:

$$\tau = \tau_w^e, \quad q_w = q_w^e \quad (4.27)$$

Boundary conditions for k and ϵ are determined from the condition of turbulence equilibrium in the near-wall computational mesh cell:

$$\frac{\partial k}{\partial y} = 0, \quad \epsilon = \frac{C_u^0.75k^{1.5}}{ky} \quad (4.28)$$

4.2.2 Thick-Boundary-Layer approach

When the number of cells across the boundary layer is more than approximately 10 Navier-Stokes calculations are performed. Turbulent boundary layers incorporate the well-known wall function, however, instead of the classical logarithmic velocity profile being used, Flow Simulation uses the full profile proposed by Van Dreist (1956):

$$u^+ = \int_0^{y^+} \frac{2.d\eta}{1 + \sqrt{1 + 4.k^2.\eta^2 \left[1 - \exp\left(-\frac{\eta}{A_v}\right)\right]^2}} \quad (4.29)$$

where $k = 0.4054$ is the Karman constant and $A_v = 26$ is the Van Driest coefficient.

Further in-depth discussion regarding numerical methods and computational examples can be found in Sobachkin & Dumnov (2014), including validation of the software against Nguyen, Luat T. et al. (1979) experimental data for a F-16 fighter.

4.3 Input Parameters for Validation (NASA)

In order to ensure the methodology will yield accurate and useful results, validation will be carried out against data provided NASA's Langley Research Center Turbulence Modelling Resource. The purpose, as stated by NASA is "to provide a central location where Reynolds-averaged Navier-Stokes (RANS) turbulence models are documented. This effort is guided by the Turbulence Model Benchmarking Working Group (TMBWG), a working group of the Fluid Dynamics Technical Committee of the American Institute of Aeronautics and Astronautics (AIAA)." (NASA 2019).

The parameters for the initial model comparison are as follows:

- NACA0012 with pointed/closed trailing edge
- k-epsilon model
- Reynolds Number approx. 6 million
- Turbulence intensity 0.052%
- Temperature 300k,

In order to evaluate an NACA0012 aerofoil of length 1m, certain conditions require recalculation. Fluid properties are derived from Çengel & Ghajar (2015). Using Equation (4.1) for Reynolds Number we can determine the inlet flow velocity as:

$$6 \times 10^6 = \frac{1.1771 \text{kg/m}^3 \times U_c \times 1 \text{m}}{1.8531 \times 10^{-5} \text{kg/m.s}} \quad (4.30)$$

hence; $U_c = 94.458 \text{m/s}$

4.4 Mesh Refinement Process

Modelling was performed using Autodesk Inventor 2020. Data points were imported from Airfoil Tools online resource that match a NACA0012 aerofoil. Points were splined and extruded to form the 3D body in accordance with the parameters calculated above for a

1m chord length. A z-axis width of 0.2m was chosen to reduce computational overhead. This was found to be the minimum required to produce accurate 3D flow results. A 1m x 1m NACA0012 aerofoil was also modelled to provide clearer visual demonstrations of 3D flow effects to readers, shown in Figure 4.5. The models were then exported as STEP files to SOLIDWORKS 2018 for analysis using SOLIDWORKS Flow Simulation.

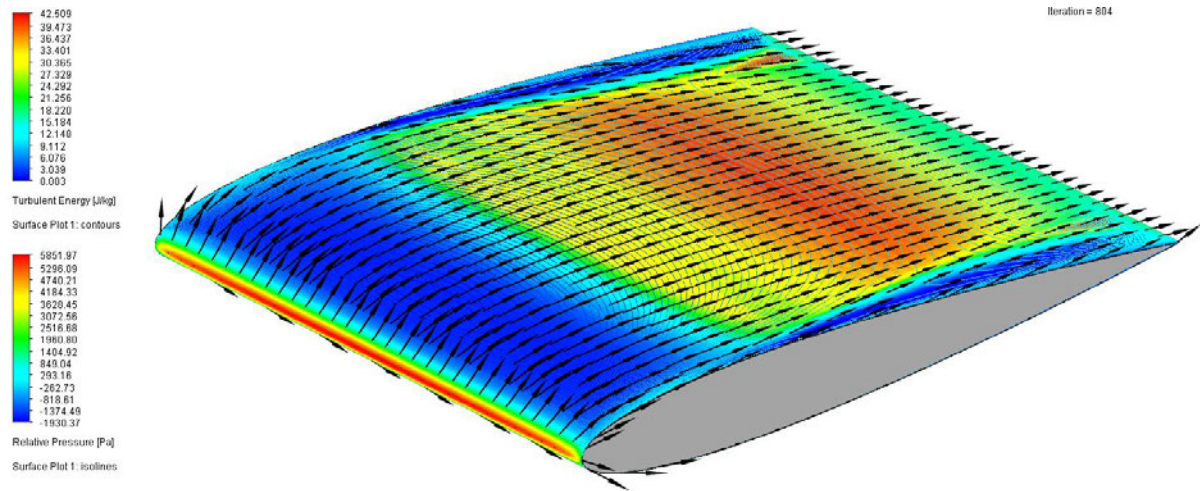


Figure 4.5: NACA0012 aerofoil (1mx1m) modelled using Airfoil Tools data, Autodesk Inventor 2020 and simulated in SOLIDWORKS Flow Simulation.

The methodology for refining and selecting an appropriate mesh for research passes through five stages of evaluation. They are:

1. Initial Mesh
2. Domain refinement
3. Global Mesh Refinement
4. Advanced Mesh Refinement
5. Final Mesh Model selection.

4.4.1 Initial Mesh

Results and accuracy vary depending upon two major aspects of the model, being the extent of the domain boundaries and the detail of the mesh, particularly in the boundary layer. Variance will be systematically reduced through multiple simulations, each model undergoing small changes until differences become negligible. An optimum level is a

model in which the computational overhead becomes most time efficient whilst yielding consistent and verifiable results.

A preliminary model has been evaluated using the calculated parameters above using generic domains and meshes to provide a starting point. One hundred refining simulations were performed. The following paragraphs detail the refinement process.

The initial basic mesh branches out with a non-uniformity meaning the mesh is biased towards the aerofoil, shown in Figure 4.6:

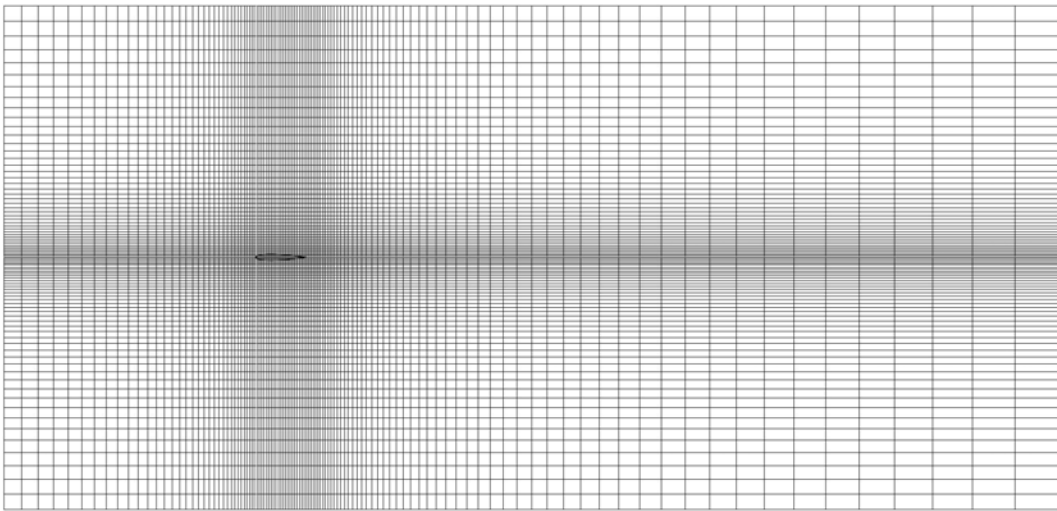


Figure 4.6: Basic, non-uniform global mesh (sectional plane x-x)

4.4.2 Domain Refinement

The fastest way to limit the cell count and thereby computational overhead is to reduce the fluid domain surrounding the aerofoil. However, an overreduction can give drastically erroneous results. By progressively increasing the boundaries forward and aft of the x-axis, the point at which further increases yields no significantly different result is considered resolved. The y-axis is similarly refined although equally in both directions due to the symmetry of the NACA0012 aerofoil.

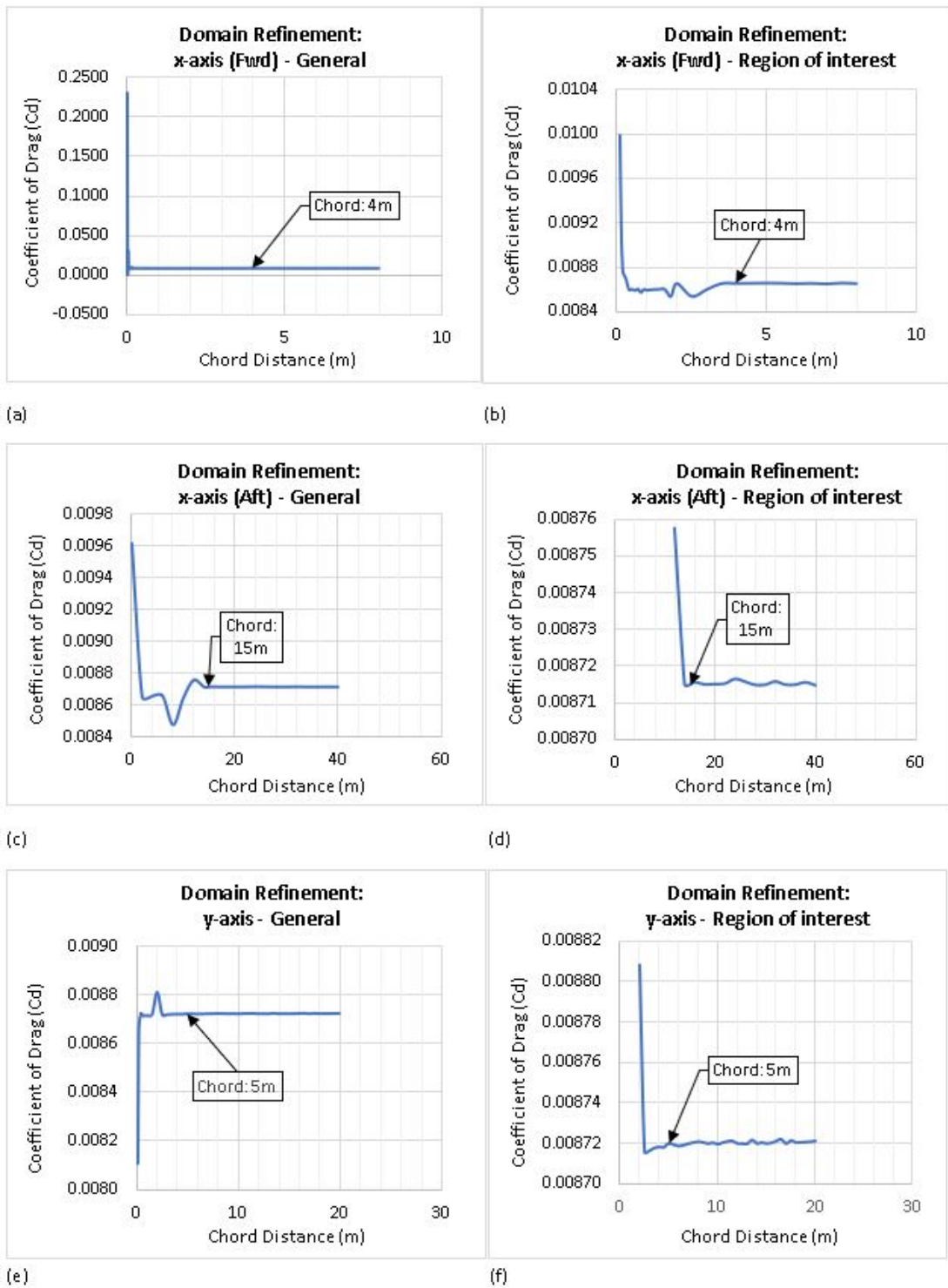


Figure 4.7: Domain refinement by boundary: general (left), specific region of interest (right)

In Figure 4.7 we see a complete view of the effect on the accuracy as the boundary distance is varied. In (a) the boundary is increased forward of the leading edge (x-axis). In (b) the region of interest from the data in (a) is zoomed in on to increase resolution of the fluctuations. This is the most significant range and selection of an appropriate boundary

value can be made. This is repeated for the zone aft of the trailing edge in the x-axis in (c) and (d) and for the y-axis boundaries in (e) and (f) respectively. Precise figures can be found in Appendix B.1 - Table B.1.

The final results indicate the optimal boundary distances to be 4m forward and 15m aft in the x-axis and 5m in both directions in the y-axis. The z-axis is set to match the width of the 3D model to reduce cell count following rigorous testing which proved that altering this boundary had no effect on results, attributed to the way in which software sets boundary conditions and calculates for wall effects.

4.4.3 Global Mesh Refinement

The software's automatic refinement of the global mesh provides a reasonably accurate approach if given sufficient iterations before consecutive refinements. It also refines only the regions necessary as opposed to manually setting an equidistant region outward from the surface, which is greatly inefficient, tremendously increasing total cell count.

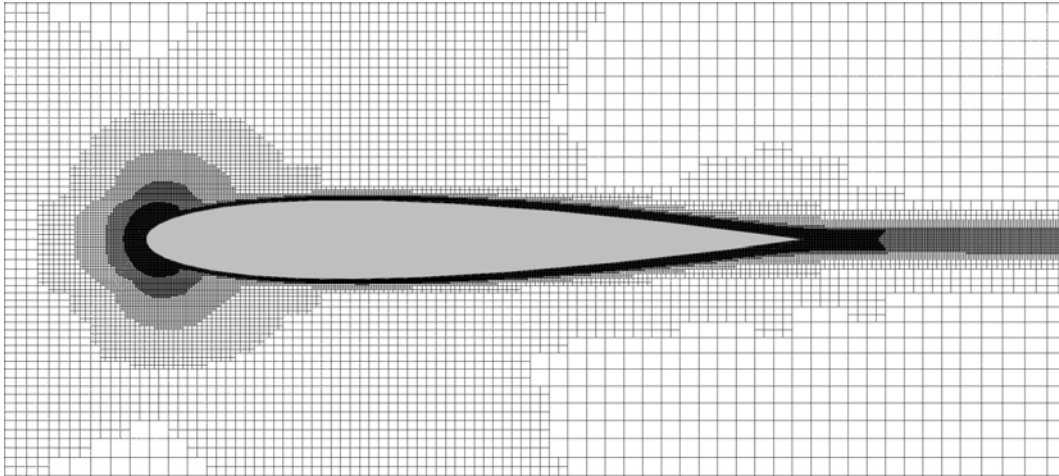


Figure 4.8: Global mesh - software auto-refinement level 6

In Figure 4.8 above, we see the efficiency in the software by allowing the basic global mesh to be automatically refined after each complete travel of the aerofoil. After 6 refinements the regions of mathematical interest are given finer resolution and increased computational power without over refining unnecessary zones. Key things to observe are the stagnation point to the front of the leading edge, the trailing flow beyond the tail and the gradual increase in the boundary layer requiring calculation from fore to aft. At this point the cell count exceeded 15 million and further refinement was beyond the computing

power available to continue. The results were measured as a percentage delta from the desired value for the coefficient of drag ($C_d = 0.00840$ as per NASA) (NASA 2019) and are shown in Figure 4.9. Again, precise values can be found in Appendix B.1 - Table B.1:

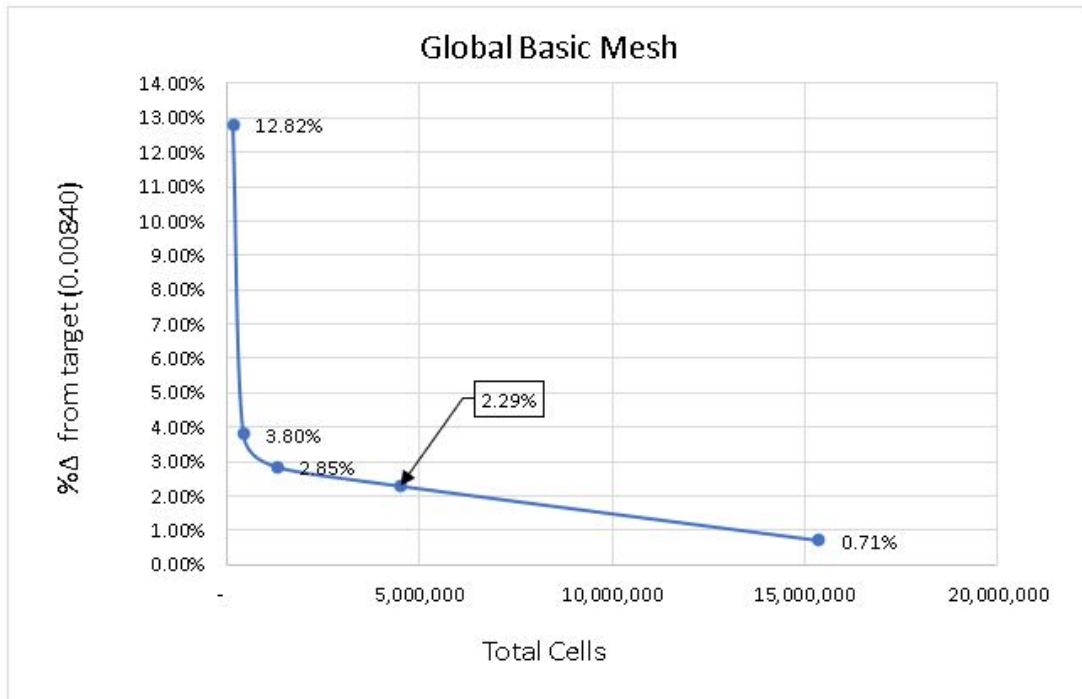


Figure 4.9: Increasing accuracy with successive global mesh refinements

Evaluating the above data suggests that a global refinement level of 4 is the optimum selection at this stage yielding a 2.29% discrepancy from the desired final value and at approximately 4.5 million cells the calculation time was also viable at 4hrs38mins. The next level jumps to approximately 15.4 million cells with a calculation time exceeding 19 hours. Whilst this is acceptable in the final model, it is impractical in this early base model as it prohibits the number of iterations that can be made to refine and improve the approach. This would decrease the long-term accuracy due to research time-constraints and so level 4 is selected for progression to advanced meshing techniques.

4.4.4 Advanced Mesh Refinement

Within the software is the ability to add local meshes to regions of interest and refine them manually. This provides greater control over the area of interest and can yield better results for similar cell counts by ignoring superfluous regions. Bespoke meshes also

provide techniques to improve particular features. In this case a local mesh will be applied to the boundary surface of the aerofoil with increased computational effort focused on the curvature of the leading edge and the tolerance level of the sharp pointed closed trailing edge with less focus on the greater space fluid domain.

The key principle to having a local mesh in this scenario is to provide the ability to manually refine advanced mesh settings at the boundary layer that will not change, whilst permitting the software to progressively and most efficiently refine the global mesh of the greater fluid domain as described earlier. Without exhaustive breakdown of the software the following summarises the criteria that will be adjusted:

1. **Curvature correction** – When the angle between the normal of two points on a curve fall below a defined value, the software will increase the resolution i.e. cell count of the mesh by dividing the cells. This will be shown to have great significance
2. **Curvature angle** – the angle specified for the curvature correction described above
3. **Tolerance level** – Sharp points below 60 degrees will undergo cell division for increased resolution, the divisions depending on the level chosen, particularly necessary for the closed trailing edge where the airflow streams off the aerofoil into the wake
4. **Immersed-body refinement** – as described above the immersed bodies represent regions where the cell is partially fluid and partially solid, this describes the cells at the boundary layer and has similarly impactful significance as curvature correction
5. **Small solid feature refinement** – this feature relates more to angles not covered by tolerance level refinements and is found to follow tolerance level results almost identically in these simulations
6. **Global basic mesh** – this is the overarching mesh focusing on the large fluid space surrounding the aerofoil.

The basic global mesh was further refined by isolating and individually simulating increases in each advanced feature. The results are shown in Figure 4.10 and 4.11:

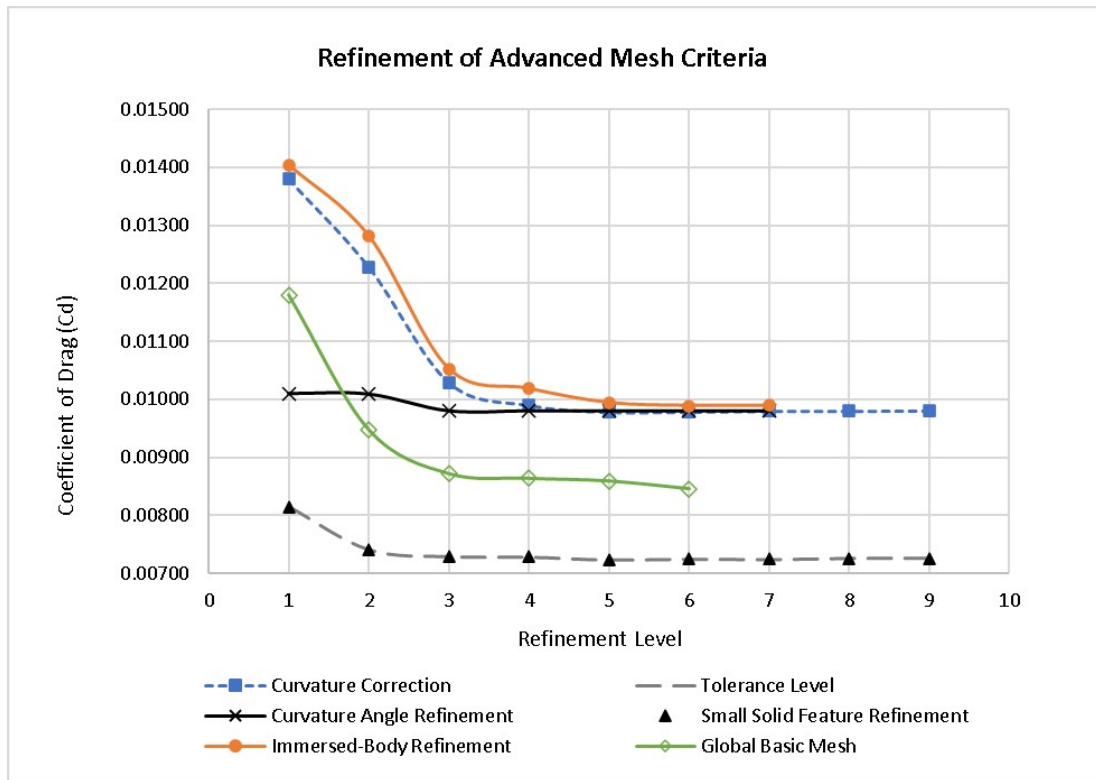


Figure 4.10: Refining specific advanced mesh criteria and the effect on the coefficient of drag

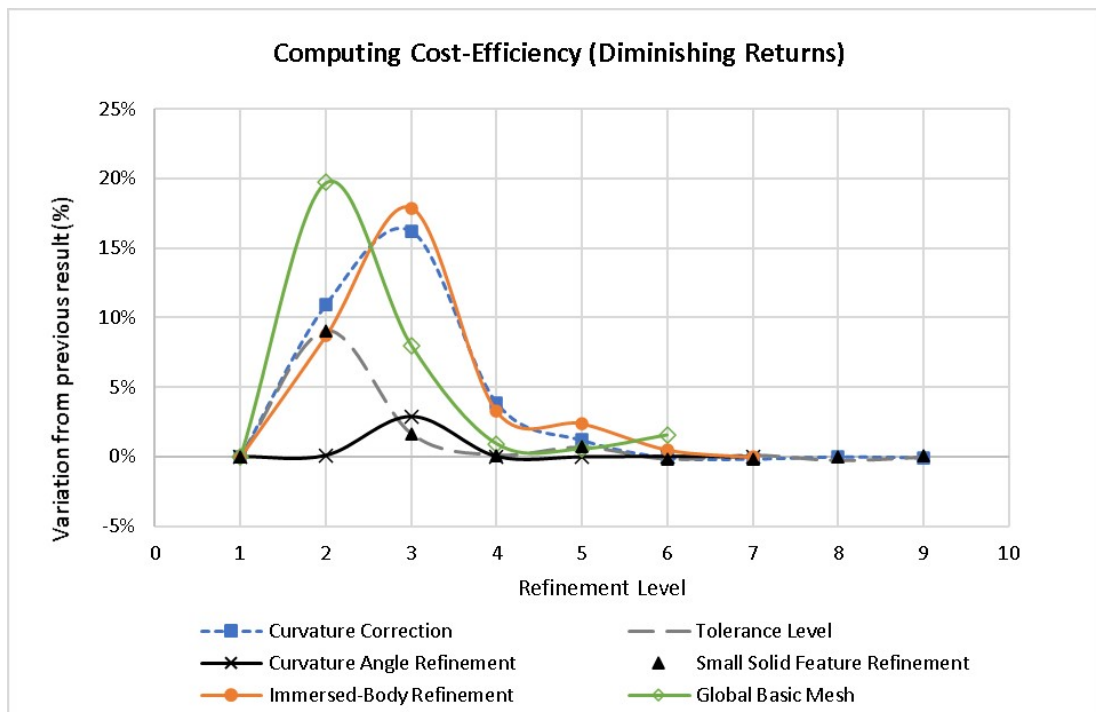


Figure 4.11: Increasing computing cost with diminishing returns

There are two scenarios in which the accuracy and computational overhead can be considered sufficient. These will undergo further analysis in section 4.4.5 and are summarised

in Table 4.1 (raw data set Appendix B.2 - Table B.2):

Table 4.1: Scenarios for comparison in selecting optimised mesh

Advanced Criterion	Moderate Values	Precision Values
Immersed-Body Refinement	5	6
Small Solid Feature Refinement	3	6
Curvature Correction	4	6
Curvature Angle Refinement	3	6
Tolerance Level	3	6
Global Mesh Refinement	1-5	1-6

4.4.5 Final Mesh Model Selection

The two scenarios in Table 4.1 were applied in two ways and compared to the global basic mesh. The first two models constrained the global mesh to manual configuration based on each of the scenarios above (moderate vs. precision values). The second models constrained only a locally applied surface mesh to the values in Table 4.1 whilst allowing the software the freedom to automatically refine the global mesh surrounding the local mesh via consecutive flow iterations.

The final mesh model selected from Figure 4.12 is FMM 1 - Global Advanced Mesh Only - Moderate Values. This model exhibits the greatest accuracy at a reasonable computational cost, allowing for the research to be completed within the given time constraints and to an acceptable level of confidence. FMM2 and FMM4 both had precision values applied. As such they require greater computing overhead from the start but tend to overshoot less. Unfortunately the next level of refinement is beyond the computational ability at hand and failed to simulate (over 40 million cells), a distinct drawback of refining already advanced meshes. FMM3 comes very close to the target but evidently corrects with additional refinement, indicating the true value is somewhere in between points 5 and 6 as the corrections/fluctuations diminish. FMM1 was able to be simulated up to 53 hours and showed very minor deviation after the 5th refinement and hence FMM1 was selected (See Appendix B.3 - Table B.3 for raw data). This was not shown in Figure 4.12 as it reduces the clarity for the other models, but is shown in Figure 4.13. This mesh

will be applied in evaluating the proposed riblet geometries explained in the next section (4.5).

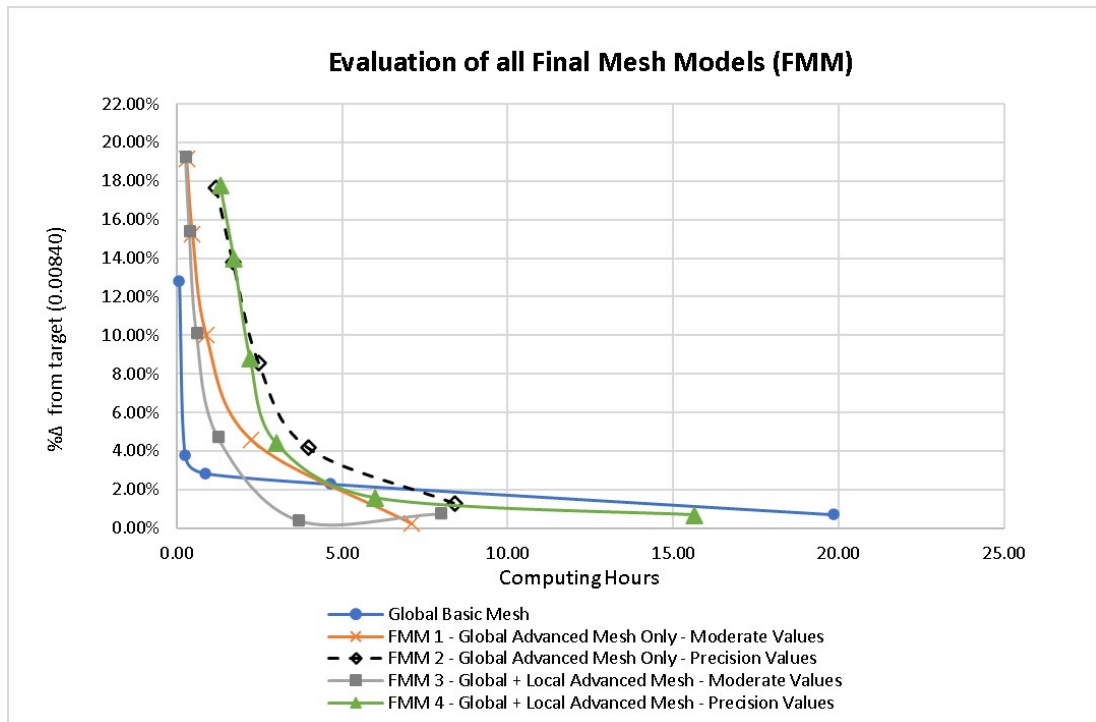


Figure 4.12: Evaluation of final mesh models with consideration to computational time

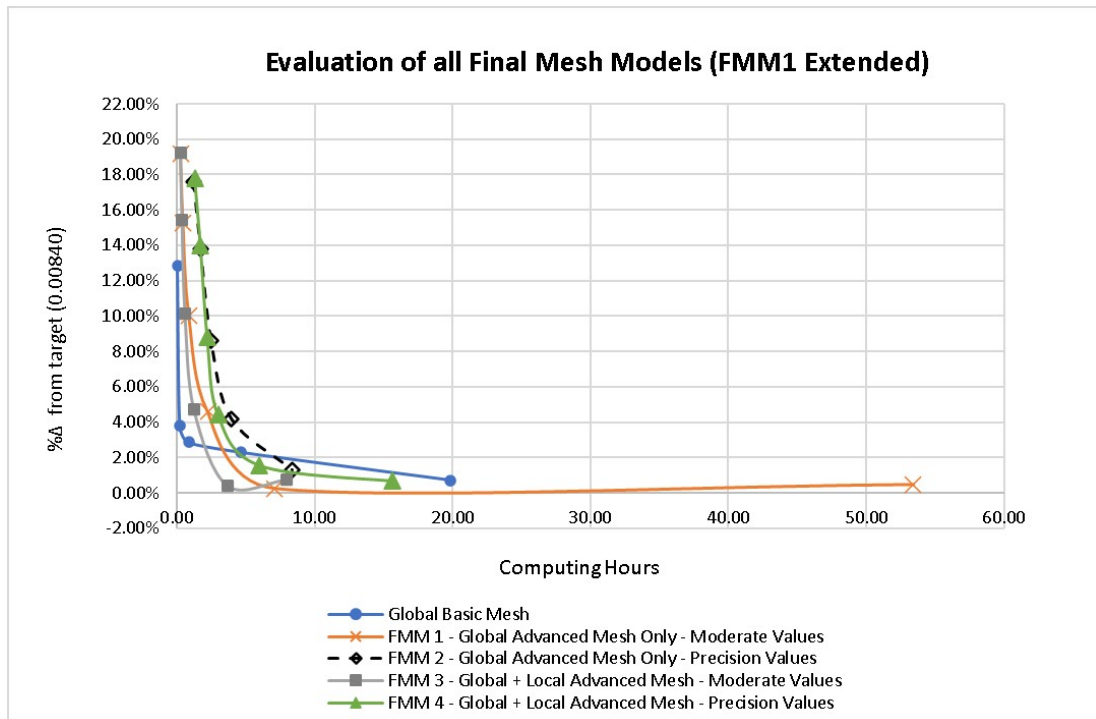


Figure 4.13: Figure 4.12 extended to show FMM1 further refinement

4.5 Proposed Research Model

In designing riblet geometry for application to the aerofoil surface, non-dimensionalised values were determined experimentally by Bixler & Bushan (2013), from which the optimum riblet spacing (s), height (h) and thickness (t) can be determined as follows:

$$s^+ = \frac{sV_t}{\nu} \quad (4.31)$$

$$h^+ = \frac{hV_t}{\nu} \quad (4.32)$$

$$t^+ = \frac{tV_t}{\nu} \quad (4.33)$$

where V_t is the wall shear stress velocity and with consideration to kinetic energy, can be derived from the wall shear stress expression $\tau_o = \rho V_\tau^2$ as:

$$V_t = \left(\frac{\tau_o}{\rho} \right)^{\frac{1}{2}} \quad (4.34)$$

The approximate wall shear stress (τ_o) is resolved through combining friction formulas for laminar and turbulent flow. The Blasius formula describes the coefficient of friction for turbulent flow as:

$$c_f = 0.0791(Re)^{-1/4} \quad (4.35)$$

The Fanning friction factor formula describes the coefficient of friction for laminar flow as:

$$C_f = \frac{2\tau_o}{\rho V^2} \quad (4.36)$$






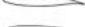







Combining the two gives the approximate wall shear stress (τ_o) as:

$$\tau_o = 0.03955v^{1/4}\rho V^{7/4}D^{-1/4} \quad (4.37)$$

Experimental results by Bixler & Bushan (2013) show that an s^+ value near 15 is optimal and $h/s = 0.5$ corresponds to approximately three riblets per vortex where vortices are thought to lift and pin to riblet tips. However, these results indicate a generally accepted value and results within experimentation for 3 and 5 m/s exhibited large ranging values of s^+ of 25.2 and 40.6 respectively (Bixler & Bushan 2013, 4511). Explicitly utilising the formulas for airflow between 5-20m/s generated riblet geometries smaller than practical for CAD modelling and simulation in this research. Additionally sawtooth or scalloped design riblets outperform blade riblets but again fail to simulate due to their increased complexity and fine detail nature at the micrometer level where computing power requirements increase exponentially.

The design parameters derived from this experimentation proved in correlation with other studies cited herein, that a $h/s = 0.5$ and a $t/s = 0.04$ performed best with height (h) varying between 25-150(μm). This is demonstrated in Table 4.2 (Bixler & Bushan 2013, 4513) :

Table 4.2: Sawtooth riblet airfoil experimentation

Reynolds number	Airfoil cross section description	Airfoil type	Sawtooth riblet size with $h = s$ [μm]	Riblets applied to longitudinal location/chord length	Trip applied to longitudinal location/chord length	Angle of attack	Maximum drag reduction
17 000	Symmetric		180	0-100%	n/a	0°	4.3%
250 000	Symmetric		23, 76, 152	10-100%	n/a	0°	13.3%
530 000-790 000	Thin		76, 152	20-95%	2.5%	0°	2.7%
750 000	Thin		114	12-96%	10%	0-6°	6%
1 000 000	Symmetric		76, 152	12-96%	10%	0-6°	13%
1 000 000	Thin		76	12-96%	10%	0-12°	10%
1 000 000	Thin		76	12-96%	10%	0-12°	14%
1 000 000	Thick		114	5-100%	5%	0°	5%
1 000 000-1 850 000	Thick		44, 62, 100, 152	40-100%	n/a	0°	5%
3 000 000	Thick		18	15-100%	6%	-0.5-1°	10%
3 300 000	Thin		17, 23, 33, 51	15-100%	n/a	0°	3.3%
2 000 000-6 000 000	Symmetric		44, 100, 152	0-100%	5%	0°	7%
4 900 000-22 300 000	n/a		33, 51, 76	87% coverage	n/a	0°	4%

For this research a simple stepped approach will see riblets varying from 25-100 μm , stepping up or down as necessary along the surface layer whilst maintaining the required spacing and thickness ($h/s = 0.5$, $t/s = 0.04$) as derived above. For example at $h = 25\mu m$, $s = 50\mu m$ and $t = 2\mu m$ and at $h = 100\mu m$, $s = 200\mu m$ and $t = 8\mu m$.

In Figure 4.14 below, we see the pressure variations along the aerofoil, noting the minimum pressure corresponding to the thinning boundary layer where the airspeed is over the aerofoil and lift generation would be greatest. Just ahead of this region is considered the rough starting point for riblet placement in the majority of studies (around 10-12% aft).

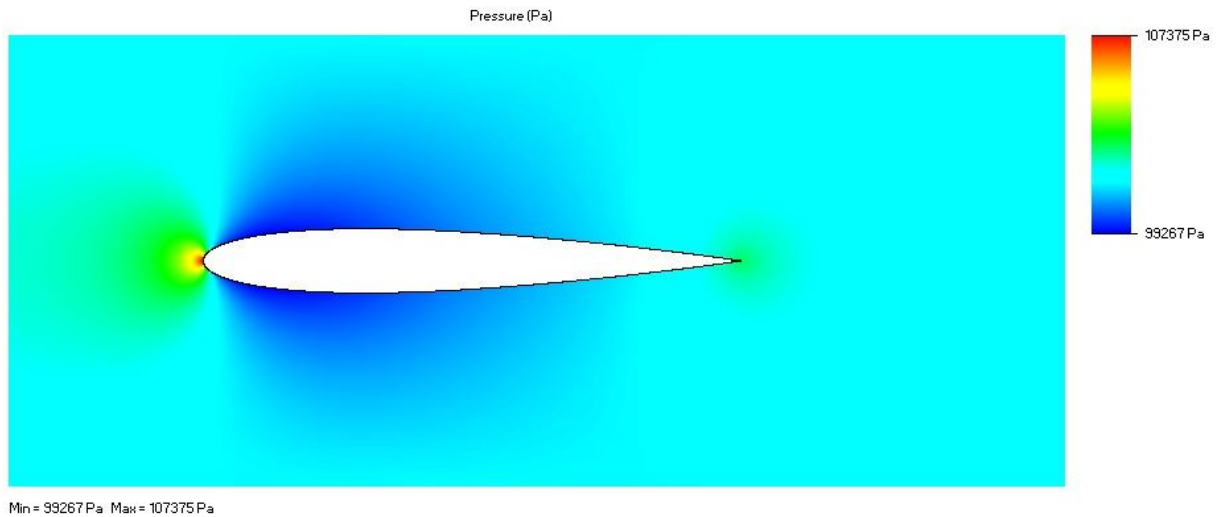


Figure 4.14: Pressure variation along chord length

In Figure 4.15 the turbulent kinetic energy increases fore to aft suggesting that varying the riblet geometry by increasing the height/protrusion into the flow along the chord may be beneficial compared to a uniform approach in capturing different sized vortex formations.

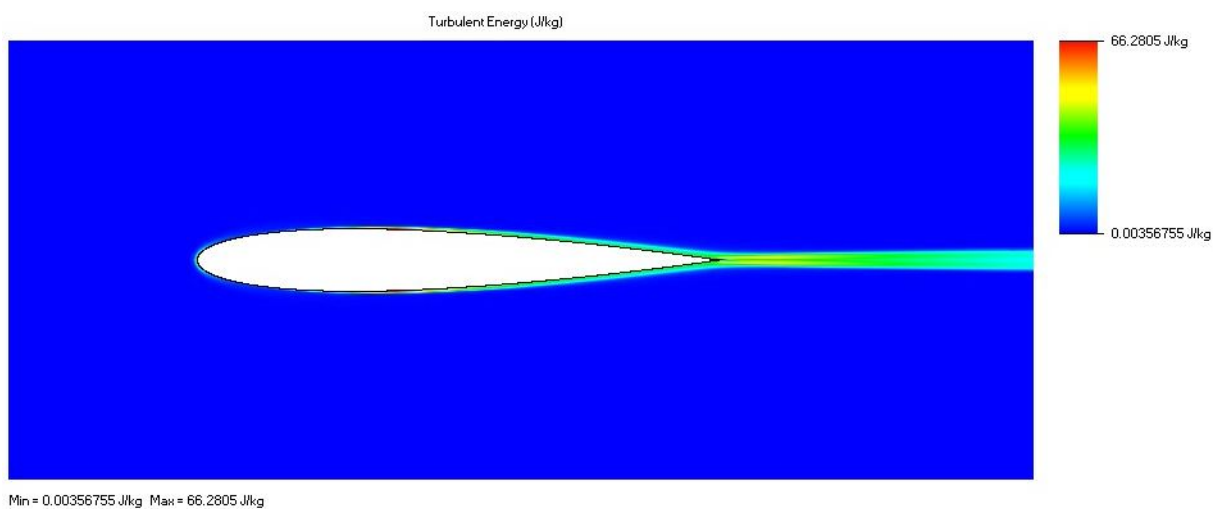


Figure 4.15: Turbulent kinetic energy along chord length

Figures 4.16 shows an example of how varying riblet heights, thicknesses and spacing

along the aerofoil surface will occur in one direction. The riblets are to scale in all except for the length, which has been shortened to fit in the image for demonstration purposes. The reverse will also be simulated.

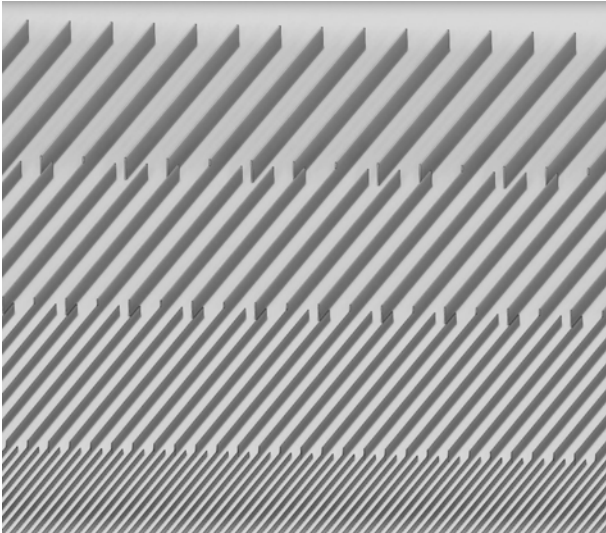


Figure 4.16: Example of non-uniform riblet design travelling chordwise along an aerofoil surface

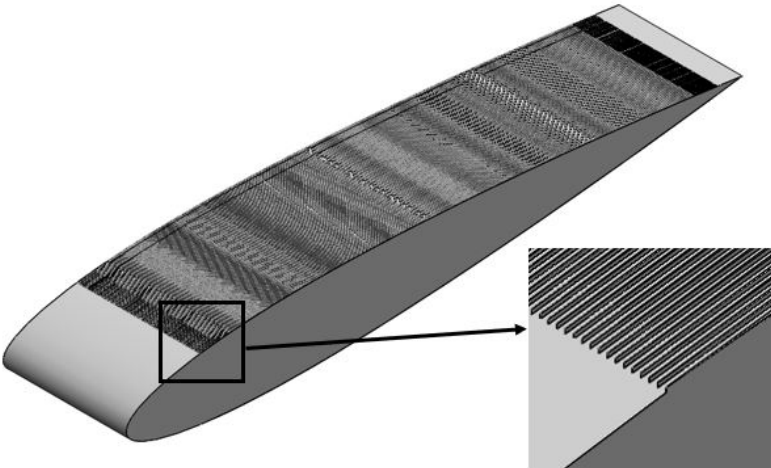


Figure 4.17: Aerofoil section with 100 μ m longitudinal riblets

Figures 4.17 above shows an example of an NACA 0012 sectional model used for simulation including the longitudinal riblets.



Figure 4.18: S-802 aerofoil section with $50\mu\text{m}$ - $125\mu\text{m}$ longitudinal riblets

4.18 Represents the S-802 wind turbine blade and is slightly more curved, particularly towards the tail than the symmetrical NACA 0012 section. The S-802 blade profile has been taken as a mid-section for evaluation in the air flow.

Chapter 5

Results and Discussion

The following results represent data gathered from numerous SOLIDWORKS Flow Simulation analyses for approximately the last 6 months of the 10 month long research. The estimated hours exceed 1,400 in computing time (with 800+ in the prior mesh optimisation stage), as once the conditions are setup the processing runs 24/7 until completed, with a queue of taskings lasting up to a week at a time. The data was then compiled in spreadsheet tables and graphed and analysed for the NACA 0012 aerofoil, before applying the same methodology to the S-802 wind turbine blade section. The results are as follows:

5.1 NACA 0012 Model

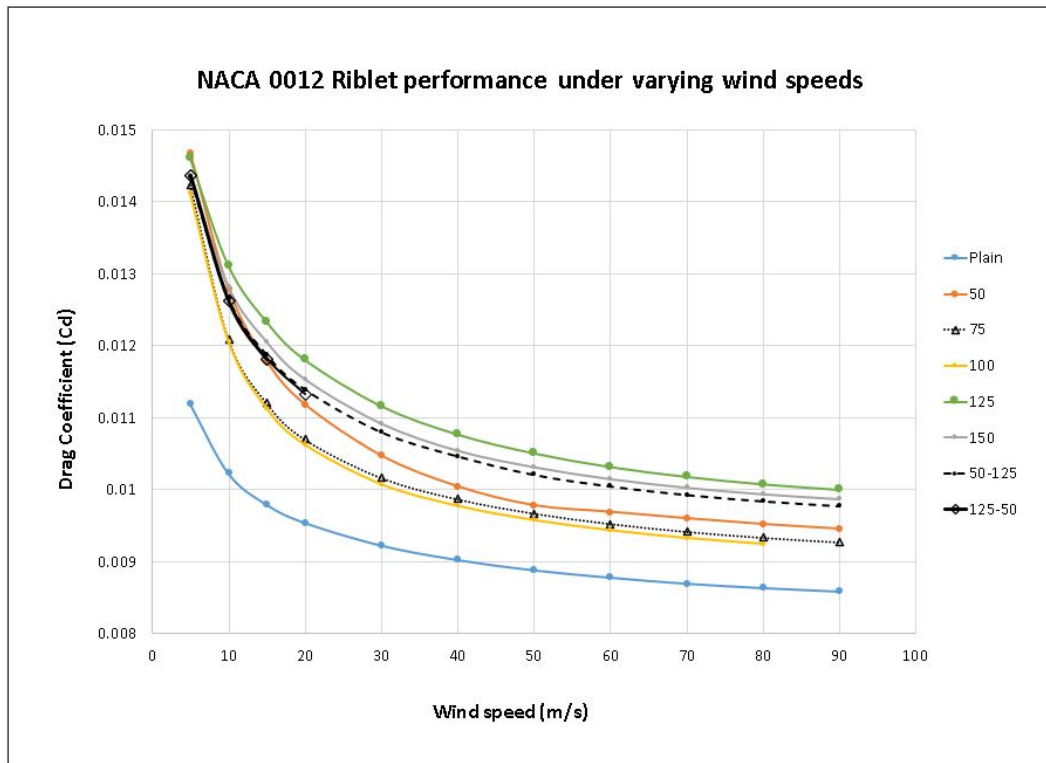


Figure 5.1: NACA 0012 Riblet performance under varying wind speeds

The results are summarised above in Figure 5.1 and detailed in Appendix B.4 - Table B.4. Wind speeds ranged from 5 to 90 m/s. The drag coefficient ranged between 0.0085 up to 0.0146. The plain aerofoil performed the best having the lowest drag coefficient approaching the NASA baseline model reaching 0.00859 at 90m/s (NASA=0.0084 at 94.458m/s). All riblet models drag coefficients were higher, delineating from one another around 10m/s and staying consistently spread up to 90m/s where the curve levels out. The 100 μ m uniform model exhibited the lowest drag of the models closely followed by the 75 μ m uniform model. The 125 μ m uniform performed the worst with $C_d = 0.01$ at 90m/s. The 50 μ m uniform model was approximately halfway at $C_d = 0.00945$ at 90m/s. Non-uniform riblet designs of 50 μ m-125 μ m and 125 μ m-50 μ m achieved nearly identical results and lay slightly higher than midway between the uniform 50 μ m and 125 μ m models. All curves remained approximately the same distance apart from one another after 20 m/s.

5.2 S-802 Wind Turbine Blade Model

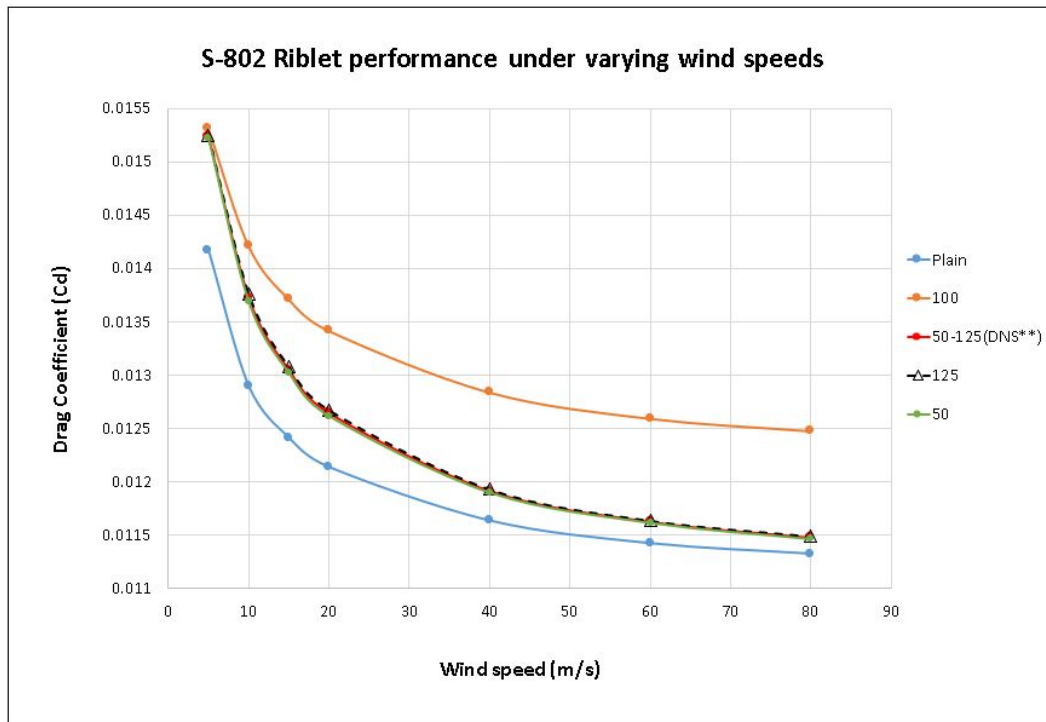


Figure 5.2: S-802 Riblet performance under varying wind speeds

The results are summarised above in Figure 5.2 and detailed in Appendix B.5 - Table B.5. Wind speeds ranged from 5 to 80 m/s. The drag coefficient ranged between 0.0113 up to 0.0153. The plain aerofoil performed the best having the lowest drag coefficient. All riblet models drag coefficients were higher. In the S-802 profile the 100 μ m uniform model performed the worst, exhibiting the greatest increase in drag. Surprisingly the 50 μ m and 125 μ m performed almost identically. The non-uniform 50-125 μ m failed to simulate during numerous trials and adjustments and so was interpolated to be in between the 50 μ m to 125 μ m values as was the case for the NACA 0012 aerofoil.

5.3 Discussion

In the NACA 0012 model all riblet models performed worse than the plain surface aerofoil which indicates the increased surface area and complexity of the shape simulates greater drag in the software as would be expected. The $100\mu\text{m}$ and $75\mu\text{m}$ uniform riblet designs performed the best of the riblet models across all wind speeds which coincides with research by Caram & Ahmed (1991) and Bixler & Bushan (2013), however did not achieve lower than the plain aerofoil as in these studies. It is likely that the software simply does not account for micrometer level vortice generation and control at the boundary layer and the approach to resolving the boundary layer is insufficient for this research. Reaf-firming this is the result of the non-uniform approaches of $50\mu\text{m}$ - $125\mu\text{m}$ and vice versa; here we see they lay roughly midway in between the uniform $50\mu\text{m}$ and $125\mu\text{m}$ results which indicates the software is likely resolving with respect to features of surface area and other minor details such as channel width and average protrusion into the flow without the ability to simulate actual vortices.

In the S-802 model the $100\mu\text{m}$ riblets performed notably worse than the $50\mu\text{m}$ or the $125\mu\text{m}$. This was an unexpected result considering the $100\mu\text{m}$ performed the best of the riblet models on the plain NACA 0012 aerofoil. A possible reasoning for this may be that the S-802, with it's increased curvature, experiences higher velocity along the boundary layer of the upper surface and thus the $100\mu\text{m}$ riblets fall within a particular region of transitional flow that the $50\mu\text{m}$ does not protrude and the $125\mu\text{m}$ entirely penetrates, causing unexpected calculations in resolving the iterations based on SOLIDWORKS Flow Simulation thin layer and thick layer boundary approach as described in sections 4.2.1 and 4.2.2.

Chapter 6

Conclusions and Further Work

6.1 Conclusions

The following objectives have been addressed:

Drag reduction using riblet microstructures The hypothesis was not proven i.e. the riblets increased the coefficient of drag (C_d) instead of reducing it in all riblet models both uniform and non-uniform. The raising, pinning, lateral separation and surface area interaction reduction in micro-vortices provides a reasonable explanation for underlying fluid mechanics but achieving simulation modelling using this particular software was not successful. It should be noted that the limitations expressed in section 3.1.2 of the research methodology apply regarding available computing power and software licensing and therefore greatly impeded the potential of the software and the study as a whole when considering simulations of complex boundary layer effects at the micrometer scale.

Non-uniform Riblet Designs Non-uniform designs did not outperform uniform riblets. The results for non-uniform riblets ranging from $50\mu\text{m}$ - $125\mu\text{m}$ and vice versa rested midway between those values for uniform riblet models in the completed simulations. It is possible that the non-uniform designs simply offer no advantage over uniform designs. However, it is more likely that the software simply does not model the phenomenon as the current understanding is insufficient to invest in for software companies targetting currently marketable broad ranging commercial applications.

The incorporation of a hypothesized model into commercial software may also lead to erroneous results in other flow simulation avenues if not yet fully understood and so may explain the lack of viability in simulating riblet microstructures at this stage, with this particular software.

6.2 Further Work

This research has highlighted the need for several avenues of research. Firstly, further practical application of non-uniform riblets to aerofoils in wind-tunnel experimentation would yield real world results to ensure the complexities of the phenomenon in drag reduction are guaranteed to occur in the research. Aspects of scaling wind turbine blades for use in wind tunnel experiments were discussed in section 2.6.2 of the literature review.

Secondly, the use of 3-D printing and prototyping provides a rich depth of research opportunity for printing micrometer scale surface features on aerofoils as well as wind tunnel testing 3-D printed models. The viability of this would include the ability to print to adequate surface roughness and whether alternative blade designs as seen in Figure 2.8 (sawtooth, scalloped, etc.) could be achieved for superior drag reduction. Whilst standard aerofoils have been printed and successfully used, there remains vast opportunity for research into stereolithography (SLA) printing to $25\mu\text{m}$ level resolution and aspects of rigidity and stability in wind tunnels.

Finally further research would look to the software simulation aspects and creating a bespoke, custom coded solution for the fluid mechanisms underlying the vortex generation, raising, pinning, separation and control to prevent entanglement on the boundary layer surface. If a software code were to be created to replicate studies cited within this research as a foundation, then applied to the same methodology herein, a simulation solution could be achieved which could then be incorporated into commercial software in the future.

References

- Abbot, I. & Doenhoff, A. (1959), *THEORY OF WING SECTIONS: Including a Summary of Airfoil Data*, Dover Publications, Inc. 180 Varick Street, New York, NY 10014, USA.
- Abdelghany, E. S., Abdellatif, O., Elhariry, G. & Khalil, E. E. (2016), ‘Naca653218 airfoil aerodynamic properties’, *Journal of Aeronautics & Aerospace Engineering* **5**(2), 1–5. DOI: 10.4172/2168-9792.1000168.
- Alfredsson, P. H. & Dahlberg, J. A. (1979), ‘A preliminary wind tunnel study of windmill wake dispersion in various flow conditions’, *Technical Note AU-1499, Part 7*. FFA, Stockholm, Sweden.
- Beniak, J., Križan, P., Šooš, L. & Matúš, M. (2018), ‘Roughness and compressive strength of fdm 3d printed specimens affected by acetone vapour treatment’, *IOP Conference Series: Materials Science and Engineering* **297**(1), 012018. DOI: 10.1088/1757-899X/297/1/012018/.
- Bhaskaran, R. (2019), ‘Big Ideas: Fluid Dynamics’, Cornell University, Ithaca, New York 14850, USA. <https://confluence.cornell.edu/display/SIMULATION/Big+Ideas%3A+Fluid+Dynamics>.
- Bixler, G. & Bushan, B. (2013), ‘Fluid drag reduction with shark-skin riblet inspired microstructured surfaces’, *Advanced Functional Materials* **23**, 4507–4258. DOI: 10.1002/adfm.201203683.
- Brief, C. (2013), *Bird death and wind turbines: a look at the evidence*, Carbon Brief Limited.
- Caram, J. & Ahmed, A. (1991), ‘Effect of riblets on turbulence in the wake of an air-

- foil', *American Institute of Aeronautics and Astronautics Journal* **29**(11), 1769–1770. DOI: 10.2514/3.10802.
- Chacón, L., Crespo, A., Enevoldesen, P., Gómez-Elvira, R., Hernández, J., Højstrup, J., Manuel, F., Thomsen, K. & Sørensen, P. (1996), 'Measurements on and modelling of offshore wind farms.', Report Risø-R-903(EN).
- Chamorro, L., Arndt, R. & Sotiropoulos, F. (2013), 'Drag reduction of large wind turbine blades through riblets: Evaluation of riblet geometry and application strategies', *Renewable Energy* **50**, 1095–1105. DOI: 10.1016/j.renene.2012.09.001.
- Chang, I., Torres, F. & Tung, C. (1995), 'Geometric analysis of wing sections', *NASA Technical Memorandum 110346*. DOI: 10.1016/j.renene.2012.09.001.
- Chen, X. (2014), 'Optimization of Wind Turbine Airfoils/Blades and Wind Farm Layouts', Doctorate dissertation, Washington University, Saint Louis, Missouri, USA. DOI: 10.1016/j.renene.2012.09.001.
- Dean, B. & Bhushan, B. (2010), 'Shark-skin surfaces for fluid-drag reduction in turbulent flow: a review', *Philosophical Transactions of The Royal Society A* **368**, 4775–4806. DOI: 10.1098/rsta.2010.0201.
- Eleni, D., Athanasios, T. & Dionissios, M. (2012), 'Evaluation of the turbulence models for the simulation of the flow over a national advisory committee for aeronautics (naca) 0012 airfoil', *Journal of Mechanical Engineering Research* **4**(2), 100–111. DOI: 10.5897/JMER11.074.
- Çengel, Y. & Ghajar, A. (2015), *Heat and Mass Transfer: fundamentals and applications 5th Edn*, McGraw-Hill Education, 2 Penn Plaza, New York, NY 10121, USA.
- Fu, Y., Yuan, C. & Bai, X. (2017), 'Marine drag reduction of shark skin inspired riblet surfaces', *Biosurface and Biotribology* **3**, 11–24. DOI: 10.1016/j.bsbt.2017.02.001.
- Garg, A., Bhattacharya, A. & Batish, A. (2016), 'On surface finish and dimensional accuracy of fdm parts after cold vapor treatment', *Materials Manufacturing Processes* **31**(4), 522–529. DOI: 10.1080/10426914.2015.1070425.
- Ge, M., Tian, D. & Deng, Y. (2016), 'Reynolds number effect on the optimization of a wind turbine blade for maximum aerodynamic efficiency', *Journal of Energy Engineering* **142**(1), 04014056. DOI: 10.1061/(ASCE)EY.1943-7897.0000254.

- Ginzburg, I. P. (1970), *Theory of Drag and Heat Transfer*, Leningrad, LGU (in Russian).
- Hansen, M. (2015), *Aerodynamics of Wind Turbines, 3rd edn*, Routledge, 2 Park Square, Milton Park, Abingdon, Oxon OX14 RN, England.
- Högström, U., Asimakopoulos, D., Kambezidis, H., Helmis, C. & Smedman, A. (1988), 'A field study of the wake behind a 2mw wind turbine', *Atmospheric Environment* **22**(4), 803–820. DOI: 10.1016/0004-6981(88)90020-0.
- Højstrup, J. (1999), 'Spectral coherence in wind turbine wakes', *Journal of Wind engineering and Industrial Aerodynamics* **80**, 137–146.
- IPCC (2012), *Renewable Energy Sources and Climate Change Mitigation: Special Report of the Intergovernmental Panel on Climate Change*, Cambridge University Press, 32 Avenue of the Americas, New York NY 10013-2473, USA. https://archive.ipcc.ch/pdf/special-reports/srren/SRREN_Full_Report.pdf.
- ISO (2002), Geometrical product specifications (gps) - indication of surface texture in technical product documentation, Standard ISO 1302:2002, International Organization for Standardization.
- Jha, S., :Gautam, U., Narayanan, S. & Dhas, L. (2018), 'Effect of reynolds number on the aerodynamic performance of naca0012 aerofoil', *IOP Conference Series: Materials Science and Engineering* **377**, 1–11.
- Johnson, G. (2006), *WIND ENERGY SYSTEMS, Electronic edn*, Dr. Gary L. Johnson, Manhattan, KS.
- Kroll, E. & Artzi, D. (2011), 'Enhancing aerospace engineering students' learning with 3d printing wind-tunnel models', *Rapid Prototyping Journal* **17**(5), 393–402. DOI: 10.1108/13552541111156522.
- Kurtulus, D. (2015), 'On the unsteady behaviour of the flow around naca 0012 airfoil with steady external conditions at re=1000', *International Journal of Micro Air Vehicles* **7**(3), 301–326. DOI: 10.1260/1756-8293.7.3.301.
- Lam, C. K. G. & Bremhorst, K. (1981), 'A modified form of the k- ϵ model for predicting wall turbulence', *Journal of fluids engineering* **103**(3), 456–460. DOI: 10.1115/1.3240815.

- Lee, S., Churchfield, M., Moriarty, P., Jonkman, J. & Michalakes, J. (2012), *Atmospheric and Wake Turbulence Impacts on Wind Turbine Fatigue Loading*, 50th AIAA Aerospace Sciences Meeting Nashville, Tennessee, 9-12 January. <https://www.nrel.gov/docs/fy12osti/53567.pdf>.
- Lee, S. & Jang, Y. (2005), 'Control of flow around a naca 0012 airfoil with micro-riblet film', *Journal of Fluid and Structures* **20**, 659–672. DOI: 10.1016/j.jfluidstructs.2005.03.003.
- Mourits, J. (2014), *BEM theory and CFD for Wind Turbine Aerodynamics*, Internship report, University of Twente, 5 Drienerlolaan, 7522 NB Enschede, Netherlands. <https://pdfs.semanticscholar.org/6a1d/3174996d977acb6aa0bfad75bd57f7513d03.pdf>.
- NASA (2019), 'Langley Research Center Turbulence Modeling Resource', . <https://turbmodels.larc.nasa.gov/index.html>.
- Nguyen, L. e. a. (1979), 'Simulator Study of Stall/Post - Stall Characteristics of a Fighter Airplane with Relaxed Longitudinal State Stability', NASA Technical Paper 1538.
- Olasek, K. & Wiklak, P. (2014), 'Application of 3d printing technology in aerodynamic study', *Journal of Physics: Conference Series* **012009**(530), 1–7. DOI: 10.1088/1742-6596/530/1/012009.
- Pearce-Higgins, J., Stephen, L., Douse, A. & Langston, R. (2012), 'Greater impacts of wind farms on bird populations during construction then subsequent operation: results of a multi-site and multi-species analysis', *Journal of Applied Ecology* **49**, 386–394. DOI: 10.1111/j.1365-2664.2012.02110.x.
- Pettersson, K. (2006), *Scaling Techniques Using CFD and Wind Tunnel Measurements for use in Aircraft Design*, Licentiate Thesis, Royal Institute of Technology, SE-100 44 Stockholm, Sweden. <https://www.diva-portal.org/smash/get/diva2:10823/FULLTEXT01.pdf>.
- Rasal, S. & Katwate, R. (2016), 'Numerical analysis of lift & drag performance of naca0012 wind turbine aerofoil', *International Research Journal of Engineering and Technology* **4**(6), 2892–2896. DOI: .
- Rasal, S. & Katwate, R. (2017), 'Numerical analysis of lift & drag performance of naca0012

- wind turbine aerofoil', *International Research Journal of Engineering and Technology* **4**(6), 2892–2896. DOI: .
- Schubel, P. & Crossley, R. (2012), 'Wind turbine blade design', *Energies* **5**, 3425–3449. DOI: 10.3390/en5093425.
- Sidhu, B., Rashdan, M., Ahmad, K. & Idris, A. (2016), 'Riblets for airfoil drag reduction in subsonic flow', *ARPJ Journal of Engineering and Applied Sciences* **11**(12), 7694–7698. DOI: .
- Siemens Gamesa (2019), *Siemens Gamesa Awarded The Largest Repowering Order To Date In North America By MidAmerican Energy*, Utilities Middle East. <https://www.utilities-me.com/news/13147-siemens-gamesa-awarded-the-largest-repowering-order-to-date-in-north-america-b>
- Sobachkin, D. & Dumnov, D. (2014), *Numerical Basis of CAD-Embedded CFD White Paper*, NAFEMS World Congress 2013.
- Stanford University (2013), 'The NACA airfoil series, AA200 course notes', Stanford University, California, USA. https://archive.ipcc.ch/pdf/special-reports/srren/SRREN_Full_Report.pdf.
- Twidell, J. & Weir, T. (2015), *Renewable Energy Resources, 3rd edn*, Routledge, 2 Park Square, Milton Park, Abingdon, Oxon OX14 45N, England.
- Tyler, C., Braisted, W. & Higgins, J. (2005), 'Evaluation of rapid prototyping technologies for use in wind tunnel model fabrication', *43rd AIAA Aerospace Sciences Meeting and Exhibit, Reno, NV* (2005-1301). DOI: 10.2514/6.2005-1301.
- Valerga, A., Batista, M., Fernandez-Vidal, S. & Gamez, A. (2019), 'Impact of chemical post-processing in fused deposition modelling (fdm) on polylactic acid (pla) surface quality and structure', *Polymers* **11**(566), 1–10. DOI: 10.3390/polym11030566.
- Van Dreist, E. R. (1956), 'On turbulent flow near a wall', *Journal of the Aeronautical Science* **23**(10), 1007.
- Vermeer, L., Sørensen, J. & Crespo, A. (2003), 'Wind turbine wake aerodynamics', *Progress in Aerospace Sciences* **3**, 467–510. DOI: 10.1016/S0376-0421(03)00078-2.
- Viswanath, P. (2002), 'Aircraft viscous drag reduction using riblets', *Progress in Aerospace Sciences* **38**, 571–600. DOI: .

-
- Yousefi, K. & Saleh, R. (2015), ‘Three-dimensional suction flow control and suction jet length optimization of naca 0012 wing’, *Meccanica* **50**(6), 1481–1494. DOI: 10.1007/s11012-015-0100-9.

Appendix A

Project Specification

ENG4111/4112 Research Project

Project Specification

For: Daniel McEvoy

Title: Drag reduction and wake mitigation in wind turbines using riblet microstructures

Major: Mechanical engineering

Supervisors: Khalid Saleh

Enrolment: ENG4111 – EXT S1, 2020
ENG4112 – EXT S2, 2020

Project Aim: To analyse the performance of several variations in riblet design along the chord length of a standard aerofoil.

Programme: Version 2, 17th March 2020

1. Simulate an NACA0012 aerofoil in ANSYS as a base reference of what to expect from the ideal aerofoil without riblets. Validate methodology against turbulence data from NASA's Langley Research Center
2. Model three additional NACA0012 aerofoils using ANSYS Fluent– one with previously studied 100µm uniform riblets and two with unique and innovative riblet profile variants incorporating design changes derived from comprehensive literature research
3. Conduct in-depth CFD analysis in line with validated methodology in step 1
4. Understand the beneficial and negative aspects of each variant and to apply this knowledge in designing an NREL wind turbine blade with riblet microstructures
5. Repeat the same CFD analysis on the innovative NREL wind turbine blade design including riblet microstructures
6. Analyse data and compare the outcomes against the original aims of this project
7. Recognize required improvements to the study and suggest further research ideas

If time and resources permit:

8. Develop and 3D print fine resolution prototypes using stereolithography
9. Perform wind tunnel testing using TUSQ wind tunnel facility
10. Compare and interpret results against simulated models

Appendix B

Raw Data Sets

The following raw data sets were collected over the previous 10 months of research using simulation software. Some have been restructured and summarised before being converted into tables for visual clarity. The true data comprises a far greater amount. This appendix hopes to add depth to the findings by incorporating only the most relevant, accurate and/or whole data sets used during the research process.

B.1 Domain Mesh Optimisation

Table B.1: Domain Mesh Optimisation Data

x-axis (fwd)			x-axis (aft)				y-axis		
Chords	Result	$\Delta\%$ Variation	Chords	Result	uniform	$\Delta\%$ Variation	Chords	Result	$\Delta\%$ Variation
0	0.22989	-	0	0.00962		-	0.1	0.00811	-
0.01	0.00293	98.72%	2	0.00865		10.04%	0.2	0.00866	-6.87%
0.02	0.03068	-945.32%	4	0.00866		-0.07%	0.4	0.00872	-0.64%
0.03	0.02165	29.44%	6	0.00866		0.01%	0.6	0.00871	0.10%
0.04	0.00861	60.22%	8	0.00848		2.09%	0.8	0.00871	-0.02%
0.06	0.00861	0.07%	10	0.00865		-1.99%	1	0.00871	0.00%
0.08	0.00854	0.79%	12	0.00876		-1.30%	1.5	0.00872	-0.05%
0.1	0.00999	-16.99%	14	0.00871		0.49%	2	0.00881	-1.05%
0.12	0.00956	4.28%	15	0.00871	0.00800	0.00%	2.5	0.00872	1.05%
0.14	0.00922	3.60%	16	0.00872		-0.01%	3	0.00872	-0.01%
0.16	0.00896	2.73%	18	0.00871		0.01%	3.5	0.00872	-0.02%
0.18	0.00885	1.24%	20	0.00872		0.00%	4	0.00872	-0.01%
0.2	0.00876	1.08%	22	0.00872		0.00%	4.5	0.00872	0.00%
0.3	0.00870	0.69%	24	0.00872		-0.01%	5	0.00872	-0.02%
0.4	0.00860	1.11%	26	0.00872		0.01%	6	0.00872	0.01%
0.5	0.00860	-0.05%	28	0.00871		0.01%	7	0.00872	-0.01%
0.6	0.00859	0.14%	30	0.00871		0.00%	8	0.00872	-0.01%
0.7	0.00861	-0.15%	32	0.00872		-0.01%	9	0.00872	0.01%
0.8	0.00858	0.35%	34	0.00871		0.01%	9.5	0.00872	0.00%
0.9	0.00860	-0.34%	36	0.00871		0.00%	10	0.00872	0.01%
1	0.00860	0.11%	38	0.00872		-0.01%	10.5	0.00872	-0.01%
1.2	0.00860	-0.08%	40	0.00871		0.01%	11	0.00872	-0.01%
1.4	0.00860	-0.01%					11.5	0.00872	0.00%
1.6	0.00860	-0.01%					12	0.00872	0.01%
1.8	0.00854	0.76%					12.5	0.00872	0.00%
2	0.00866	-1.37%					13	0.00872	0.00%
2.5	0.00854	1.34%					13.5	0.00872	-0.02%
3	0.00860	-0.73%					14	0.00872	0.02%
3.5	0.00866	-0.62%					14.5	0.00872	-0.01%
4	0.00866	-0.01%					15	0.00872	0.01%
4.5	0.00866	-0.02%					15.5	0.00872	0.00%
5	0.00866	-0.02%					16	0.00872	-0.01%
5.5	0.00866	0.02%					16.5	0.00872	-0.01%
6	0.00865	0.05%					17	0.00872	0.02%
6.5	0.00866	-0.04%					17.5	0.00872	-0.02%
7	0.00865	0.06%					18	0.00872	0.01%
7.5	0.00866	-0.09%					18.5	0.00872	0.00%
8	0.00866	0.05%					19	0.00872	0.00%
							19.5	0.00872	0.00%
							20	0.00872	0.00%

Table B.1 is a record of useful data during the domain refinement process. The highlighted selections indicate where further refinements began to exhibit negligible benefits on the resultant drag coefficient. These were therefore selected as optimum cost versus accuracy values for the final mesh design.

B.2 Advanced Mesh Criterion Optimisation Data

Table B.2: Advanced Mesh Criterion Optimisation Data

Global Basic Mesh							
Global Mesh Level	Boundary Layer Mesh Level	Total Cells	Iterations	Time (hh:mm:ss)	Result	Variation	%Δfrom target
1	1	80,828	239	0:1:56	0.011801	-	40.48%
2	2	176,603	352	0:4:37	0.009476	19.696%	12.82%
3	3	449,868	507	0:14:56	0.008719	7.993%	3.80%
4	4	1,322,404	730	0:51:40	0.008639	0.913%	2.85%
5	5	4,517,200	1404	4:38:12	0.008593	0.541%	2.29%
6	6	15,399,267	1887	19:51:05	0.008460	1.546%	0.71%

Curvature Correction							
Global Mesh Level	Curvature Level	Total Cells	Iterations	Time (hh:mm:ss)	Result	Variation	%Δfrom target
1	1	54,857	1523	0:11:47	0.013796	-	64.24%
1	2	56,000	1538	0:12:07	0.012285	10.952%	46.25%
1	3	58,372	1567	0:12:55	0.010293	16.217%	22.54%
1	4	62,665	1619	0:14:43	0.009897	3.849%	17.82%
1	5	69,757	1699	0:17:33	0.009779	1.187%	16.42%
1	6	84,652	1845	0:24:42	0.009785	-0.054%	16.48%
1	7	113,771	2079	0:39:59	0.009799	-0.142%	16.65%
1	8	168,048	2427	1:11:14	0.009798	0.010%	16.64%
1	9	275,363	2925	2:29:22	0.009804	-0.063%	16.71%

Curvature Angle Refinement							
Refinement Level	Curvature Angle (deg)	Total Cells	Iterations	Time (hh:mm:ss)	Result	Variation	%Δfrom target
1	18	68,923	845	0:8:26	0.010098	-	20.21%
2	17	69,153	846	0:8:28	0.010088	0.095%	20.10%
3	16	69,757	850	0:8:31	0.009796	2.900%	16.62%
4	15	69,757	850	0:8:32	0.009795	0.008%	16.61%
5	14	69,757	850	0:8:28	0.009797	-0.020%	16.63%
6	13	69,757	850	0:8:32	0.009795	0.021%	16.61%
7	12	69,757	850	0:8:39	0.009796	-0.011%	16.62%

Immersed-Body Refinement							
Global Mesh Level	Immersed-Body Refinement Level	Total Cells	Iterations	Time (hh:mm:ss)	Result	Variation	%Δfrom target
1	1	55,992	770	0:06:04	0.014035	-	67.08%
1	2	63,252	813	0:07:03	0.012815	8.691%	52.56%
1	3	92,280	490	0:06:15	0.010525	17.871%	25.30%
1	4	208,872	525	0:15:36	0.010182	3.259%	21.21%
1	5	664,332	394	0:42:32	0.009939	2.387%	18.32%
1	6	2,503,236	617	5:01:52	0.009889	0.506%	17.72%
1	7	9,890,736	976	44hrs+	0.009891	-0.023%	17.75%

Table B.2: Advanced Mesh Criterion Optimisation Data (continued)

Tolerance Level							
Global Mesh Level	Tolerance Criterion	Total Cells	Iterations	Time (hh:mm:ss)	Result	Variation	%Δfrom target
1	1	54,546	664	0:4:49	0.008147	-	-3.01%
1	2	54,714	1005	0:8:4	0.007409	9.059%	-11.80%
1	3	55,092	1274	0:09:08	0.007288	1.633%	-13.24%
1	4	55,974	1346	0:10:21	0.007280	0.110%	-13.33%
1	5	57,612	404	0:03:12	0.007231	0.673%	-13.92%
1	6	61,140	1062	0:08:55	0.007245	-0.194%	-13.75%
1	7	67,692	1254	0:11:58	0.007238	0.097%	-13.83%
1	8	79,788	1010	0:11:51	0.007259	-0.290%	-13.58%
1	9	103,980	1883	0:30:40	0.007262	-0.041%	-13.55%

Small Solid Feature Refinement							
Global Mesh Level	Tolerance Criterion	Total Cells	Iterations	Time (hh:mm:ss)	Result	Variation	%Δfrom target
1	1	54,546	760	0:05:35	0.008146	-	-3.02%
1	2	54,714	761	0:05:36	0.007408	9.065%	-11.81%
1	3	55,092	762	0:05:38	0.007288	1.627%	-13.24%
1	4	55,974	766	0:05:42	0.007283	0.067%	-13.30%
1	5	57,612	774	0:05:58	0.007232	0.691%	-13.90%
1	6	61,140	789	0:06:43	0.007246	-0.192%	-13.74%
1	7	67,692	816	0:07:56	0.007260	-0.185%	-13.58%
1	8	79,788	1293	0:15:25	0.007260	-0.003%	-13.57%
1	9	103,980	1415	0:22:42	0.007258	0.024%	-13.59%

Table B.2 contains the data produced in refining the advanced criterion of the mesh manually. Again as the diminishing returns reached an optimum value these were selected to produce both a 'moderate' value option and a 'precision' value option for testing and selection of which would be the most research effective final model with light to time constraints and available computing power.

B.3 Final Mesh Model Refinements

Table B.3: Final Mesh Model Optimisation Data

FMM 1 - Global Advanced Uniform Mesh Only - Moderate Values							
Global Mesh	Boundary Mesh	Total Cells	Iterations	Time	Result	Variation	%Δfrom
Nil	Moderate Values	239,124	272	0:10:47	0.010009	-	19.15%
1	Moderate Values	270,610	413	0:17:44	0.010011	-0.017%	19.18%
2	Moderate Values	418,646	572	0:28:31	0.009682	3.279%	15.27%
3	Moderate Values	896,571	770	0:53:28	0.009242	4.553%	10.02%
4	Moderate Values	2,433,834	1043	2:15:24	0.008785	4.938%	4.59%
5	Moderate Values	7,146,311	1426	7:06:35	0.008420	4.159%	0.24%
6	Moderate Values	20,162,164	1971	5:25:24	0.008438	3.954%	0.45%

FMM 2 - Global Advanced Mesh Only - Precision Values							
Global Mesh	Boundary Mesh	Total Cells	Iterations	Time	Result	Variation	%Δfrom
Nil	Moderate Values	721,154	539	1:02:35	0.009878	-	17.60%
1	Moderate Values	832,679	622	1:12:02	0.009880	-0.020%	17.62%
2	Moderate Values	961,451	839	1:42:32	0.009558	3.263%	13.78%
3	Moderate Values	1,490,763	1082	2:28:42	0.009121	4.569%	8.58%
4	Moderate Values	2,746,451	1372	3:58:02	0.008749	4.073%	4.16%
5	Moderate Values	6,690,167	1752	8:24:36	0.008507	2.776%	1.27%

FMM 3 - Global + Local Advanced Mesh - Moderate Values							
Global Mesh	Boundary Mesh	Total Cells	Iterations	Time	Result	Variation	%Δfrom
Nil	Moderate Values	235,932	272	0:11:26	0.010015	-	19.22%
1	Moderate Values	250,478	410	0:16:39	0.010016	-0.010%	19.23%
2	Moderate Values	321,962	557	0:23:24	0.009695	3.201%	15.42%
3	Moderate Values	584,028	731	0:36:15	0.009249	4.596%	10.11%
4	Moderate Values	1,523,456	965	1:15:18	0.008796	4.901%	4.72%
5	Moderate Values	4,390,915	1289	3:40:36	0.008436	4.099%	0.42%
6	Moderate Values	10,310,710	1295	7:59:24	0.008465	-0.344%	0.77%

FMM 4 - Global + Local Advanced Mesh - Precision Values							
Global Mesh	Boundary Mesh	Total Cells	Iterations	Time	Result	Variation	%Δfrom
Nil	Enhanced Values	777,204	410	0:55:16	0.009881	-	17.63%
1	Enhanced Values	784,596	616	1:19:24	0.009894	-0.131%	17.78%
2	Enhanced Values	824,139	825	1:44:10	0.009573	3.236%	13.97%
3	Enhanced Values	973,666	1042	2:13:26	0.009138	4.545%	8.79%
4	Enhanced Values	1,535,052	1287	3:00:11	0.008771	4.021%	4.41%
5	Moderate Values	3,608,242	1847	5:59:47	0.008532	2.729%	1.57%
6	Moderate Values	10,303,707		15:39:06	0.008457	0.876%	0.68%

Table B.3 contains the data produced in refining the Final Mesh Model options. In this data the 'moderate' and 'precision' values from both the Domain and Advanced Mesh optimisations were input and simulated to evaluate several final model configurations, again for time versus accuracy reconciliation.

B.4 NACA 0012 Riblet Performance

Table B.4: NACA 0012 Riblet Performance Data

		Riblet Height (μm)							
		Plain	150	125	100	75	50	50-125	125-50
Velocity (m/s)	5	0.01119	0.014357	0.014604	0.0141116	0.01423	0.014675	0.01434	0.014361
	10	0.010227	0.012823	0.013115	0.0120613	0.012089	0.012788	0.012656	0.012616
	15	0.009794	0.012058	0.012335	0.0111289	0.011203	0.011785	0.011878	0.011815
	20	0.009542	0.011541	0.011809	0.010625	0.010699	0.011184	0.011395	0.011331
	30	0.009226	0.010924	0.011166	0.0100739	0.010164	0.010472	0.010801	DNS
	40	0.009025	0.010547	0.010772	0.0097734	0.009868	0.010043	0.010466	DNS
	50	0.008882	0.010318	0.010509	0.0095756	0.00967	0.00978	0.010209	DNS
	60	0.00878	0.010152	0.010319	0.0094339	0.009526	0.009688	0.010048	DNS
	70	0.008696	0.010032	0.010183	0.0093267	0.009417	0.009599	0.00993	DNS
	80	0.008635	0.009941	0.010079	0.0092453	0.009334	0.009518	0.009841	DNS
	90	0.008586	0.009873	0.010003	DNS	0.00927	0.009454	0.009774	DNS

****DNS = Did Not Simulate (Terminated abnormally or unable to finish)**

Table B.4 contains the data produced in simulating all riblet models on the NACA 0012 aerofoil section. Some values represented by DNS in the table were unable to completely simulate, encountering abnormal termination or unknown errors likely related to computing power limitations in memory or procesing. These were left out if not fully completed to maintain accuracy of the known values.

B.5 S-802 Riblet Performance

Table B.5: S-802 Riblet Performance Data

		Riblet Height (μm)				
		Plain	125	100	50	50-125(DNS)**
Velocity (m/s)	5	0.0141702	0.0152472	0.0153138	0.015224	0.0152356
	10	0.0128978	0.0137631	0.0142104	0.0136899	0.0137265
	15	0.0124097	0.0130763	0.0137101	0.0130188	0.01304755
	20	0.0121336	0.0126704	0.0134147	0.0126145	0.01264245
	40	0.0116309	0.0119277	0.0128365	0.0118969	0.0119123
	60	0.011418	0.0116343	0.0125905	0.0116125	0.0116234
	80	0.0113193	0.0114877	0.0124739	0.0114609	0.0114743

****DNS = Did Not Simulate (Terminated abnormally or unable to finish)**
Interpolated values based on NACA 0012 results

Table B.5 contains the data produced in simulating all riblet models on the S-802 aerofoil section. 50-125 μm values (**DNS) in the table were unable to completely simulate, encountering abnormal termination or unknown errors likely related to computing power limitations in memory or processing. Data was interpolated based on the NACA 0012 findings.